For what it's worth, I hope it was worth all the while…

Analysis of Retinal Angiogram Images

A Thesis submitted in partial fulfillment of the
requirements for the degree of

Master of Science (by Research)
in
Computer Science

by

B. R. Siva Chandra
200307001
sivachandra_br@students.iiit.ac.in

International Institute of Information Technology
Hyderabad, INDIA
November, 2005

This thesis document is submitted to the **International Institute of Information Technology**, Hyderabad, INDIA as a partial fulfillment of the requirements for the degree of **Master of Science by Research** in **Computer Science**.

The work presented here was supervised by **Dr. Jayanthi Sivaswamy**. This work was done at the **Center for Visual Information Technology** of the International Institute of Information Technology, Hyderabad, INIDA in collaboration with the **LV Prasad Eye Institute**, Hyderabad, INDIA.

Images of the retina, presented in this thesis, have been acquired from the LV Prasad Eye Institute, Hyderabad, INDIA, with prior permission to use, present and make multiple copies (electronic and paper).

INTERNATIONAL INSTITUTE OF INFORMATION TECHNOLOGY

Hyderabad, INDIA

CERTIFICATE

I certify that the work presented in this thesis was done by B. R. Siva Chandra under my supervision as partial fulfillment of the requirements for a degree of MS by Research in Computer Science. This work is original and has not been submitted anywhere else as thesis.

Dr. Jayanthi Sivaswamy
Associate Professor
International Institute of Information Technology
Hyderabad, INDIA

Date:

Acknowledgements

There are a number of individuals who had to guide me for the two years I spent over my thesis. Firstly, I thank my supervisor, Dr. Jayanthi Sivaswamy, for being patient and understanding. The freedom she gave me, and the confidence and trust which she bestowed on me, made the two years a comfortable experience. I thank Dr. Tara Prasad Das of the LV Prasad Eye institute for his trust and ever positive reviews which kept my confidence levels high. I would also like to thank Dr. C. V. Jawahar, under whom I worked as a teaching assistant during the my first semester. He showed me as to what one means by 'Worshiping Work'. I thank Mr. Mohan Ram of the LV Prasad Eye Institute who had to put up with my tendancy to 'gate-crash' into his office and demand attention. He had the patience to teach opthalmology to a technologist.

Lastly, but in the most superior way, I thank my parents, my brother, and my ailing grandmother, for always believing that I was working on something worth-while.

Abstract

Diabetes is occuring in an ever increasing percentage of the human population. Though generally non-fatal, it can lead to diseases of other vital organs of the human body. *Diabetic Retinopathy* (DR) is one such disease which affects the human retina. If not treated in time, the affected patient can lose his/ her sight. With a growing number of patients affected with diabetes, the need is for fast and automatic computer aided tools which can aid in the diagnosis of DR. Currently, DR is diagnosed by a manual analysis of retinal angiogram images (RAIs). This process is tedious and depends on the subjective perception of the doctors and technicians. In this thesis, we propose a modular framework for computer aided analysis of RAIs which can be used to build analysis systems which can automatically detect diseases like the DR and assign an objective measure to the extent of the disease. The framework consists four independent modules: 1) The Pre-processing Module - For rectification of the problems and defects affecting a RAI; 2) The Structure Analysis Module - For extraction of the structure of the retina; 3) The Disease Analysis Module - For extracting the candidate regions affected by a particular disease; 4) The Classification Module - For classifying the candidate 'disease-regions' into true positives and false positives. Depending on the desired output, one can choose to incorporate some or all of these modules into the analysis system.

Non-uniform illumination is a common problem affecting RAIs and needs to be addressed. A technique for correcting non-uniform illumination forms a part of the pre-processing module. In this thesis, a technique for illumination correction, which models the illumination effect as a multiplicative degradation, is presented.

The most important of the structural features of the retina are the blood vessels. Blood vessels can be detected by modeling them as topographic ridges. In this thesis, a novel curvature estimation technique is presented, using which a ridge detection algorithm is formulated for single scale as well as multiple scales.

DR leads to two different kinds of pathologies in the human retina. These are: a.) Microaneurysms, (MAs) and b.) Capillary Non-Perfusion (CNP). In this thesis, a novel curvature based technique for detection of MAs is presented. Likewise, a novel technique for segmentation of regions of CNP, from RAIs obtained using a laser camera, is presented. This segmentation technique uses a special property of the images obtained using a laser camera.

To showcase the proposed framework, a tool called the 'CNP Analyser' that was developed is presented. This tool can detect the regions of CNP from RAIs obtained using a laser camera. The proposed illumination correction technique and the CNP segmentation technique are incorporated into this tool. A measure of the extent of CNP is derived using the percentage area of the regions of CNP.

Contents

List of Figures

Chapter 1. Introduction

1.1. Diabetic retinopathy

The fast pervading corporate culture has led to increased occurance of diabetes in the human population. It is estimated that there are 18.2 million people in the United States, or 6.3% of the population, who have diabetes [1]. India has the dubious distinction of having the largest number of diabetic patients with more than 30 million people diagnosed with diabetes [6]. Diabetes, though generally non-fatal, can affect other vital organs of the human body. If not treated in the early stages, the organs affected by diabetes can malfunction or completely stop functioning.

Diabetic retinopathy (DR), as the name suggests, is a disease of the human retina caused by diabetes. It is diagnosed by observing the extent of two different kinds of defects on the retina: (1) *Micro-aneurysms*, and (2) regions of *capillary non-perfusion.* Microaneurysms are 'sprouts' of newly developing blood vessels in the retina. On the other hand, regions of capillary non-perfusion are regions where the capillary network in the retina stops supplying blood to the corresponding areas. If not treated in time, regions of CNP can spread across the areas of the retina. When such a spread enters the central region of the retina (which is responsible for most of human vision, see Section 2.1), the patient can go blind. Microaneurysms are defects occuring in the early stages of DR, while CNP is a defect occuring in the later stages of DR.

1.2. The need for computer aided analysis of retinal angiogram images

The treatment for DR varies from simple drug based cures to laser surgeries depending on the stage at which the disease is first detected and the manner in which it progresses in a patient. Clinically, the disease is diagnosed manually by visually analysing the *angiogram images* of the retina. Because of this, the diagnosis and treatment of the disease become dependent on the subjective perception of the doctors and technicians involved. With a growing number of patients affected with diabetes, efficient disease management has also become an important issue that needs to be tackled. The need is for fast computer aided diagnostic tools for detection of the disease. Not only should such tools help in detection and diagnosis, but should also be able to remove the operator subjectivity and assign an objective measure to the extent of the disease. A computer aided system can also help in tracking the progress of the disease, under treatment or otherwise. Accurate tracking will help in developing a better understanding of the disease and develop precise treatment procedures. Disease tracking is beyond the scope of this thesis.

In this thesis, we present a general framework for computer aided analysis of retinal angiogram images. The framework can be used to build image analysis systems which can automatically detect and quantify pathologies of the retina like DR from angiogram images. The image analysis system is broken down into a number of modules which sequentially process the input image to extract information at different levels. A detailed description of the framework is presented in Chapter 3.

1.3. Organisation of the thesis

In the next Chapter (Chapter 2), we present detailed descriptions of the retinal imaging systems and the corresponding clinical procedures for the detection of CNP in the human retina. In Chapter 3, the proposed framework for the analysis of retinal angiogram images is presented. The framework consists of four modules. Specific instances of these modules are presented in Chapters 4 to 7. To showcase the framework, a tool called the 'CNP Analyser' has been developed. This is presented in Chapter 8. The thesis ends with a summary, and list of directions (Chapter 9) for continuing the work on retinal angiogram image analysis.

Chapter 2. Background

2.1. The human retina

A cross-sectional diagram showing the various parts of a human eye is shown in Figure 2.1. Retina is the sensory membrane that lines most of the large posterior chamber of the vertebrate eye [7]. A diagram of the retina in particular is shown in Figure 2.2. This figure shows two main 'land-marks', namely the **Macula** and the **Optic-Disk**, of a retina. The macula is a circular region in the center of the retina with the **Fovea** as its central core [16]. It is generally a dark/dull region devoid of any vasculature and is responsible for most of human vision. In particular, it is responsible for the central vision and houses the photo-receptive cells called the cones [23].

The optic-disk (OD) is a bright disk like structure through which the blood vessels and the neural network enter the retina. For a human eye, there exist two sides: i) Nasal side, which is the side close to the nose; ii) Temporal side, which is the side close to the temple. OD is located on the nasal side of the macula. In a retinal image of a left eye, the OD appears to the left of the macula, and in a retinal image of the right eye, OD appears to the right of the macula. The distance between the center of the optic-disk and the macula is normally two-and-a-half times the diameter of the optic-disk.

The tentacular structure in Figure 2.2 represents the prominent vasculature in the retina. Below the retinal layer is a **'Choroidal'** layer (shown in Figure 2.1), which has its own vasculature. Most of this thesis limits itself to the retinal layer except in few rare instances when attention is drawn to choroidal layer explicitly.

2.2. The basic retinal imaging procedure

The human eye has a circular opening called the *pupil* (see Figure 2.1) through which light enters the eye and reaches the retina. Retinal imaging systems use this opening to capture the image of the retina. The diameter of the pupil adjusts itself so as to let an optimum amount of light enter the eye. However, the pupil can be 'dilated' using drugs in order to obtain a large diameter, irrespective of the amount of light entering the eye. Often, in order to facilitate better illumination of the retina, the patient's eyes are dilated before capturing the images.

As can be seen in Figure 2.1, the human retina has the shape of an inner surface of a hemishpere. Because of this, it is not possible to capture the entire retina in a single image. Different parts are imaged by making the patient look in different directions, or by aiming the camera in different directions. Typically,

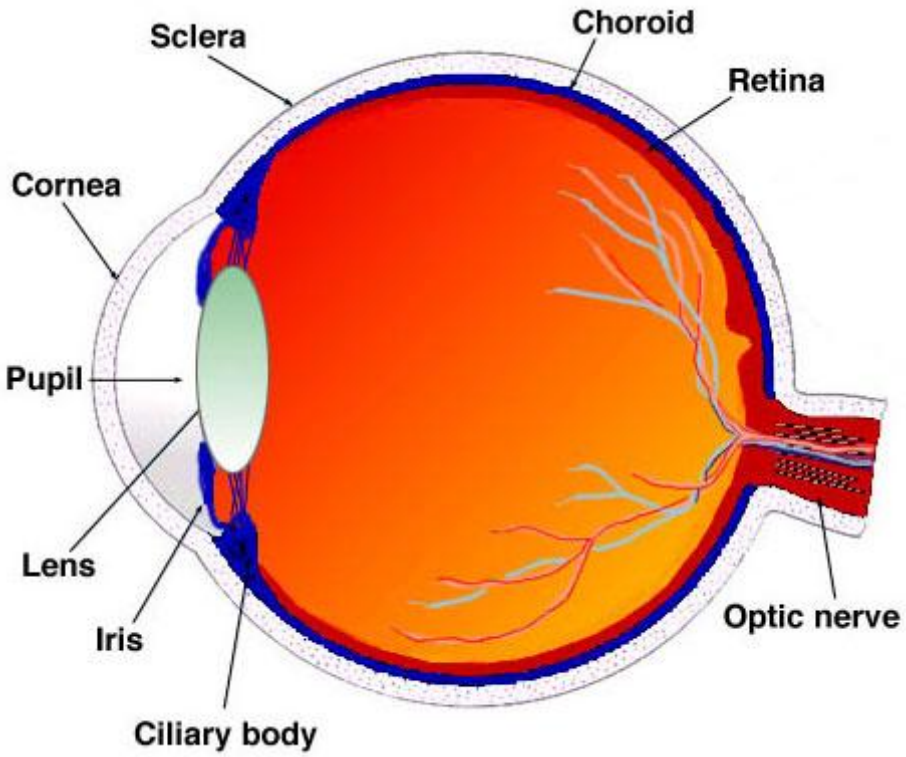

Figure 2.1. Anatomy of a human eye.

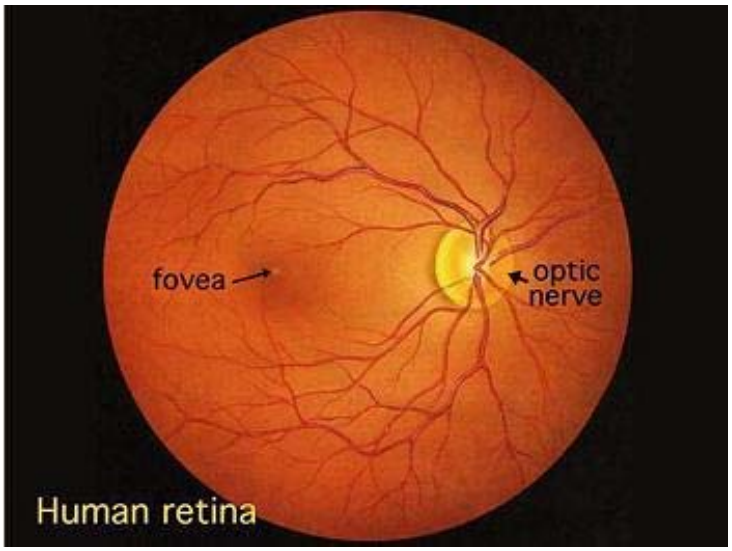

Figure 2.2. A human retinal image.

depending on the field of view of the camera, a number of images are obtained so that the part of the retina that is of interest is captured in at least one image.

2.3. Retinal angiography

Diagnosis of many diseases of the retina, like the diabetic retinopathy, require the study of perfusion of blood through the different parts of the retina. The images obtained using the procedure outlined in Section 2.2 are insufficient for such a study as the path of the blood flow cannot be traced using such images. A different class of images, called the retinal *angiogram* images are used to understand the flow of blood in the retina.

Angiogram images are obtained by a procedure called **Angiography**. It is a clinical procedure performed to study the perfusion (or the flow) of blood through the vasculature in a particular organ or region of a human body. In short, it is a technique used to trace the path of the blood. An angiography of the retina is performed as follows. First, the patient's pupils are dilated. Next, a flourescent dye is injected into the circulatory system of the patient's body. The patient's blood acts as a carrier for this dye, carrying the dye to only those regions of the retina which are recieving the blood supply. Normally, it takes around 15 seconds, from the time of injection, for the dye to reach the retina if it is injected into the hand. After this short duration, images of the retina are obtained using a particular wavelength of light. These images are called **retinal angiogram images**. The technical name for a retinal angiogram is **Fundus Flourescene Angiogram** (FFA). For the rest of the thesis, we shall refer to a retinal angiogram image as an FFA image. All FFA images are gray-scale images. An example of an FFA image is shown in Figure 2.3. Regions receiving normal blood supply appear as bright white regions and regions lacking in blood (due to abnormal supply of blood) appear as dark regions.

Each region of the retina has its own characteristic manifestation in an angiogram image. Figure 2.3 shows an angiogram image with the different regions of the retina marked. Below is a list of these regions and a brief description of their manifestations in an FFA image.

- **Macula**

  Macula is the physical center of the retina. It appears as a dark circular region with increasing brightness towards the periphery. The 'thinness' of the vascular network in the macular region causes the dark texture. The center of the macula, called the **fovea**, is devoid of vasculature.

- **Optic-disk**

  Optic-disk (OD) is the opening through which the blood vessels and the neural network enter and leave the retina. It typically appears as a bright circular disk like object on the nasal side of the macula.

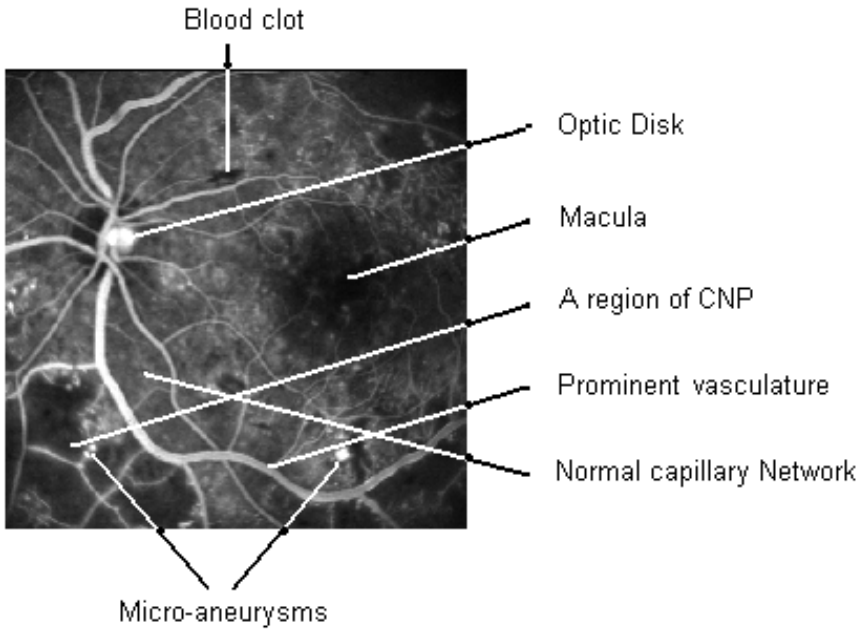

Figure 2.3. Retinal artifacts as seen in a FFA image.

- **Blood vessels**

  The large blood vessels appear as bright, hose like structures in an FFA image. In most central images of the retina, one can observe two prominent vessels emerging out of the optic-disk in a parabolic shape. These are called the 'arcades'.

- **Capillary Network**

  A normal, healthy capillary network in the retina appears as grey/white region with a woolly texture in an FFA image.

- **Regions of CNP**

  Regions of CNP appear as dull/dark lesions bounded by healthy vasculature and capillary network. They appear dark because of the fact that the dye does not perfuse into such regions. They fail to exhibit flourescence of a healthy region and are called regions of hypo-flourescence.

- **Regions of hyper-flourescence**

  Sometimes, due to diabetes or other diseases, the blood vessels weaken or rupture (hemmerhages). Blood constantly effuses out of such weak or ruptured vessels. As the effusing blood contains the injected dye, such regions appear as excessively bright, white regions and are called as regions of hyper-flourescence.

- **Blood Clots**

  When blood effusing out of a ruptured vessel clots, the region of the retina under such clots is blocked from the view of the camera. Such regions appear as dark regions and are called as regions of blocked-flourescence.

- **Microaneurysms**

  To compensate for the occurance of a CNP, the body grows new capillaries. The early stage of such neo-vascularisation is a spherical microscopic balooning from the old vessels called a microaneurysm. Such a structure has a permeable membrane from which the dye effuses out. Microaneurysms occur as tiny spherical objects in an FFA image.

2.4. Retinal imaging systems

There are various kinds of retinal imaging systems manufactured by different companies. Images obtained from a particular system have their own characteristic properties. The work presented in this thesis uses images obtained from two different imaging systems. One imaging system is manufactured by the Carl Zeiss company [35] and uses an optical camera to capture retinal images. We shall refer to FFA images captured using this system as Zeiss images. The other system is manufactured by the Heidelberg Engineering company [14] and uses a laser camera to capture images. We shall refer to images captured using this system as HRA images (HRA for **H**eidelberg **R**etinal **A**ngiogram). Zeiss and HRA images differ with respect to size and quality, which is discussed next.

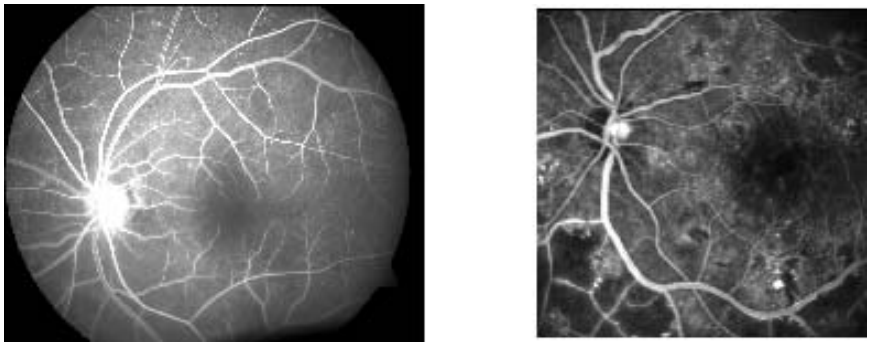

(a) (b)

Figure 2.4. (a) A typical Zeiss image. (b) A typical HRA image.

2.4.1. HRA images

HRA images are of size 512×512 pixels and are commonly corrupted by sandy/grainy noise. The

laser camera of the HRA system can penerate through the retinal layer and image the choroidal layer. Because of this, the choroidal capillary network can also be seen through regions of CNP in the image. A sub-sampled example of an HRA image is shown if Figure 2.4(b).

2.4.2. Zeiss images

The Zeiss images are of size 1280×1024 pixels. They are much less noisy as compared to HRA images, and have a smooth texture. A sub-sampled version of a Zeiss image is shown in Figure 2.4(a). The retinal regions are captured within a circular region as can be seen in the image. This circle corresponds to the aperture of the camera of the Zeiss the imaging system. The choroidal capillary network, which is visible through regions of CNP in the HRA images, is not visible in Zeiss images as the Zeiss system uses an optical camera.

2.5. Problems in retinal angiogram image analysis

Most retinal images suffer from defects which are patient dependent. In a few rare cases, the defects are also caused due to the limitations of the imaging system. Apart from these defects, there are many other problems which an FFA image analysis system has to tackle in order to deliver reliable results over a wide variety of images. Such problems, which are relevant to this thesis, are discussed in the following sub-sections.

2.5.1. Non-uniform illumination

There are many practical issues, such as the amount of dilation of the patient's eye, patient's eye movement etc., which can lead to images having spatially varying illumination. Apart from practical difficulties, there is a fundamental problem which can lead to non-uniform illumination, namely, the curvature of the retina. Because of this inherent curvature, the images capturing the peripheral regions of the retina are poorly illuminated. Likewise, images of the central regions of the retina are poorly illuminated at the peripheries. A detailed treatment of the problem of non-uniform illumination, including solutions, is presented in Chapter 4.

2.5.2. Variation in image appearance across patients

Each patient's eyes are different and hence, the maximum achievable dilation varies from patient to patient. Different degrees of dilation leads to different levels of illumination of the retina across patients. Moreover, few patients have diseases like the cataract which obstructs the path of the light into the retina. Such an obstruction leads to dullness and poor illumination of the captured image even if the degree of dilation of the pupil is adequate.

2.5.3. Different pathological regions have similar appearance

Blood clots and regions of CNP, both appear as dull/dark regions. They differ in a very subtle fashion and in most cases do not differ in appearance at all. The distinction in such cases is made based on not just the intensity values and texture, but also on the surroundings of these regions. Another example of two different pathologies having same appearance are microaneurysms and small hemmerhages. They both appear as small, excessively bright, disk like objects.

2.5.4. Dependence of the quality of the image on the time elapsed after the injection of the dye

As mentioned earlier in Section 2.3, the injected dye leaks (or effuses) out through the ruptures and weak vessels in the retina. This leaking dye creates a bright white blot on the image. The size of the blot is dependent on the amount of dye effused, which in-turn depends on the time elapsed since the injection of the dye. Apart from leakage from ruptures, the dye also effuses out from the microaneurysms and the normal vasculature. Hence, a late image (late in the sense that the image was captured after a long time after the injection of the dye) appears cloudy with bright white regions around ruptures and weak vessels.

2.5.5. Corruption by noise

Most imaging systems are not ideal and the images obtained from them are commonly corrupted by noise. The amount of noise added depends on the imaging technique used. In case of FFA images, the laser camera of the HRA system adds much more noise than the optical camera of the Zeiss system. Noise affects the textural appearance of the various parts of the retina and can lead to wrong diagnosis by both computer based systems as well as retina experts.

2.6. Summary

A retinal image is captured through the pupil in the human eye. A raw retinal image is not sufficient to trace the blood path and one requires an retinal angiogram image for this purpose. Angiogram images of the retina are obtained after injecting a flourescent dye into the patients body. Though the imaging conditions are clinically controlled, retinal angiogram images (or FFA images) suffer from many problems. These problems induce defects into the images and pose various challenges for an FFA image analysis system. The system needs to solve these problems and incorporate analysis techniques which are insensitive to the induced defects. In the next chapter, we propose such a framework for FFA image analysis, using which robust disease detection systems can be built.

Chapter 3. Framework for Retinal Angiogram Image Analysis

3.1. Introduction

An image analysis system is typically broken down into many modules with each module processing the image sequentially at different levels. The role and design of the modules depends on the particular domain of interest (which in this thesis is retinal angiogram images) and the desired output. Ideally, the system should be designed such that the processing and analysis in each module is done in a progressive manner, with the last module in the sequence yielding the desired information. With such a design, the specifications and role of the modules can be crisply defined, leading to independent and focussed design of each module. In this chapter, we propose such a modular framework for retinal angiogram image (FFA image) analysis.

3.2. Framework

Commonly, a retinal angiogram image analysis system aims to extract an objective measure of the extent and severity of a particular disease of interest. Such systems are built to serve as diagnostic aids. They can either be automatic systems which perform a complete diagnosis without the help of an expert, or can be semi-automatic systems which have a provision to let an expert correct their results.

An analysis system will have to deal with the external problems mentioned in Section 2.5. These problems can be solved in three ways:

1. The incorporated analysis techniques are designed in such way that they are insensitive to variations caused by these problems. This is an ideal case which is hard to achieve in practice. However, if one can come up with such analysis techniques, then the system can be made completely automatic.

2. The analysis techniques have an inbuilt parameter which deals with these problems. Example of such a parameter is the size of the mask in mask-based analysis techniques which can be varied to result in the desired amount of noise rejection. A system incorporating such techniques should be made semi-automatic so that an expert can set the desired values of the parameters.

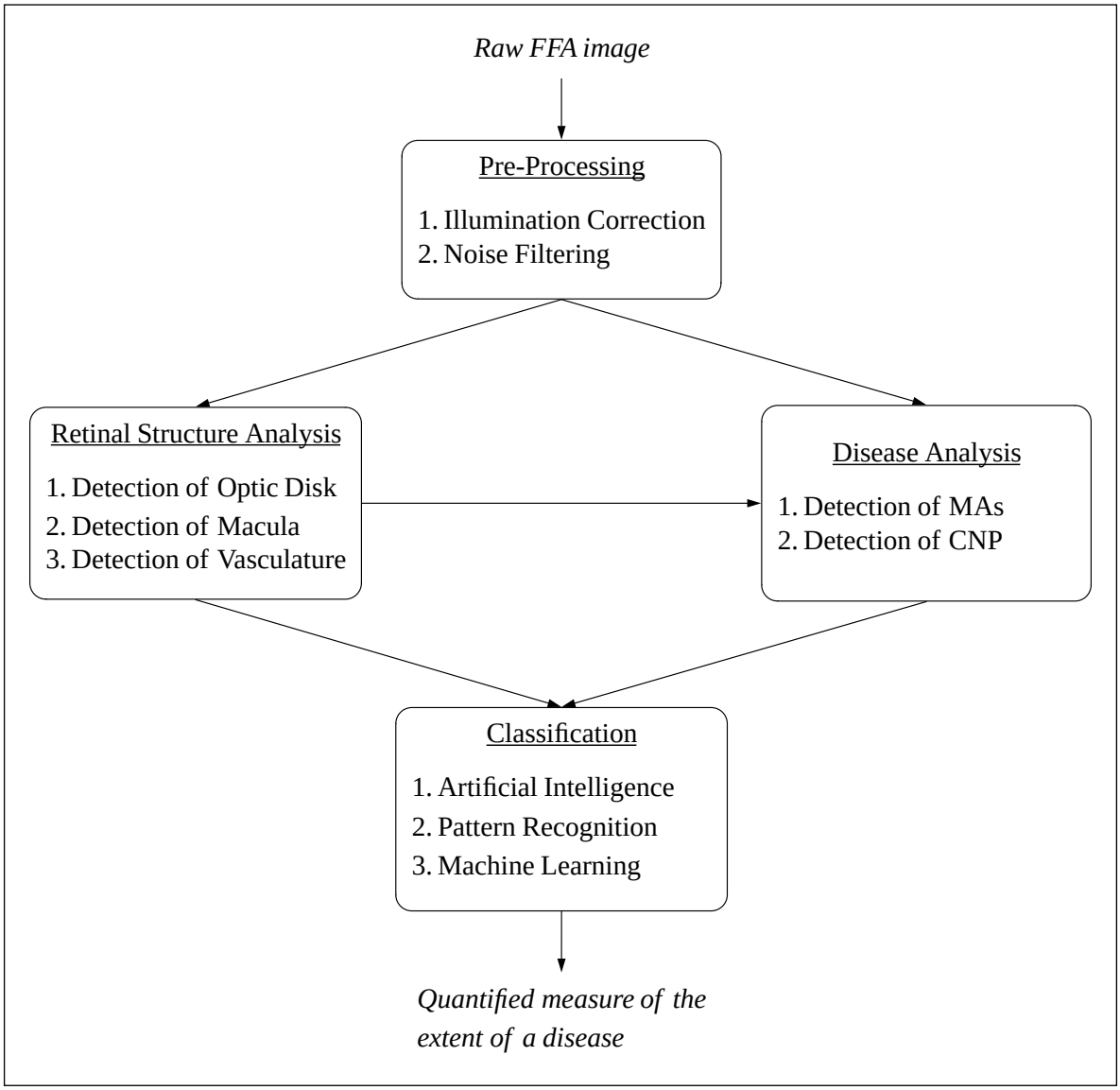

Figure 3.1. A block diagram of a typical retinal angiogram image analysis system.

3. A separate pre-processing module should be incorporated into the analysis system. This module should solve some or all of the problems, independent of the kind of analysis technique used. A system incorporating such a module can either be made completely automatic or can be made semi-automatic.

In general, image analysis techniques are developed using a certain model (heuristic or analytical) for the features of interest. An efficient analysis technique will have to be insensitive to variations in the features, such as shape, size, etc. Adding the external variations, induced by the problems mentioned in

Section 2.5, will further compound the problem making the design of the analysis techniques harder. If a system is designed such that the external problems are solved in a separate module before an analysis of the images, then the design of the analysis techniques need not take the external variations into account. Hence, we propose such a framework for retinal image analysis wherein there exists a separate pre-processing module before an analysis of the image. The block diagram of the complete framework is shown in Figure 3.1. Addition of a pre-processing module is same as following the option 3 from the above list. Moreover, it allows the analysis system to incorporate options 1 and 2, if possible/required.

An FFA image can be considered to have two different kinds of features namely, **a) Retinal Structure Features** and **b) Disease Features**. Retinal Structure features refer to sub structures of the retina. Examples of such features are optic disk, blood vessels, macula etc. Disease features are those which occur due to the damage caused by a retinal disease. Examples of such features are regions of CNP, microaneurysms etc. An analysis of FFA images will either extract the retinal structure features, or the disease features (or disease regions). Hence, following the pre-processing step is a structure analysis module or a disease analysis module (see Figure 3.1). Optionally, a disease analysis module can use the information extracted by the structure analysis module. This is indicated by an arrow from the structure analysis module to the disease analysis module in Figure 3.1. Ideally, the disease analysis module should aim to detect all candidate disease regions (in the rest of the thesis, the phrases 'disease features' and 'disease regions' will be used interchangeably).

An image analysis technique is based on an analytic property of the feature of interest. It generally does not make use of higher level knowledge. Hence, the features detected after an analysis step need not all be the desired features. The analysis step should be followed by another step which validates the detected features. Specifically, this step should classify the detected features into two sets, true positives or false positives. This classification step is indicated as the last step in Figure 3.1.

In the following subsections, we discuss few of the possible contituents of the various modules in context of the work presented in this thesis.

3.2.1. Pre-processing module

The pre-processing module typically consists of operations such a noise removal, illumination correction etc. In the case of Zeiss images, there exists another important pre-processing operation. The retinal regions in these images are captured within a circular aperture. In order to confine operations to this circular area, the first processing step is to calculate the center and radius of this aperture. In this thesis, we present two different pre-processing operations: 1) Extraction of the center and radius of the circular aperture in Zeiss images (addressed in Appendix B); 2) An Illumination correction technique for any FFA image (addressed in Chapter 4).

3.2.2. Retinal structure and disease analysis modules

Retinal structures of interest in an FFA image are the optic disk, blood vessels, macula etc. In this thesis, detection of blood vessels is addressed in Chapter 5. Diseased regions of interest in an FFA image are regions of CNP, microaneurysms etc. In this thesis, detection of microaneurysms is addressed in Chapter 6, and detection of regions of CNP is addressed in Chapter 7.

3.2.3. Classification module

The regions extracted by the disease analysis module are candidate regions affected by a particular disease. As mentioned earlier, these regions need not all be true diseased regions. The classification module classifies these regions into true diseased regions and non-diseased regions. The techniques used in this module are typically formulated using principles from fields like pattern recognition, machine learning, and artificial intelligence. The work presented in this thesis pertains only to image analysis techniques. Classification of candidate regions is beyond the scope of this thesis.

3.3. Building an FFA analysis system

Based on the various needs of an FFA analysis system, a modular framework was proposed in the previous section. Often, a system need not make use of all the modules. Depending on the formulation of the analysis techniques and the desired output, one can opt not to use one or more of the modules in Figure 3.1. On the other hand, every system will have to incorporate a pre-processing module to perform illumination correction or noise filtering. In this section, we present few examples of construction of FFA analysis systems using the proposed framework to illustrate when and how one would use the different modules.

3.3.1. System for detection of microaneurysms

As mentioned in Section 2.3, microaneurysms appear as tiny disk like objects in an FFA image. Hence, locating disk like objects will detect all candidate microaneurysms in an FFA image. An analysis technique which detects disks will form a part of the disease analysis module. However, the detected disks will have to be validated as true microaneurysms and false microaneurysms. This validation has to be done by a classification module. These steps do not require the structural information of the retina, and hence, a structural analysis module is not required. Only three modules: the pre-processing module, disease analysis module and the classification module will form the complete analysis system.

3.3.2. System for detection of regions of CNP

A CNP detection system should first identify the candidate regions of CNP. This is a function of the

disease analysis module. Next, these candidate regions have to be validated by the classification module as true diseased regions and false diseased regions. The classification can be done using the guiding principle that a region of CNP has to be bounded by prominent vasculature on at least one side. Hence, the classification module can make use of the structural information of the retina, which in this case is the location of blood vessels. Therefore, the analysis system has to incorporate all the four blocks of the proposed framework.

Chapter 4. Illumination Correction

4.1. Introduction

Most retinal images suffer from non-uniform illumination despite the controlled conditions under which imaging takes place. Some of the reasons for this were briefly mentioned in Section 2.5. They are repeated here for convenience.

a. The retina is a curved surface and hence all the retinal regions cannot be illuminated uniformly. The pupil through which the retina is illuminated is at the center of the eyeball and hence, the amount of light illuminating the peripheral regions of the retina is much less compared to the the central regions.

b. The imaging is done with the patient's pupil dilated and the degree of dilation is highly variable across patients. A wider pupil will allow more light to enter the patient's eye and hence illuminate the retina better.

c. The bright flash-light used to illuminate the retina makes the patient move his/her eye away from the veiw of the camera involuntarily.

d. Presence of other diseases such as cataract can block the light from reaching the retina.

Most computer based image analysis techniques require tuning of parameters to suit a particular application and feature of interest. If the image appearance/properties vary widely across different images, the tuning of these parameters will have to be done for every image leading to a loss in robustness of the analysis system. Correcting the effects of non-uniform illumination before performing an analysis will alleviate the problem of parameter tuning and increase the robustness of the analysis system. Similarly, removing the effects of non-uniform illumination can also improve disease diagnosis by human experts. Hence, correcting the effects of non-uniform illumination is important for the analysis of FFA images by both human experts as well as computers.

The desirable characteristics for an illumination correction (IC) technique are as follows.

1. IC is a low-level technique and should not depend on high-level information such as the knowledge of the location of the sub-structures of the retina. This is because, the extraction of sub-structures is generally a higher level processing step and is influenced

by the variation in illumination.

2. IC should be performed without any manual intervention for parameter tuning.

3. IC should not affect the fidelity of the image as this can adversely influence diagnosis by human experts.

In this chapter, we present an IC technique which is based on modelling the illumination as a multiplicative effect on the original image and has the desired characteristics listed above. Before presenting this technique, we shall present a brief review of common techniques for IC.

4.2. Background

Images suffering from non-uniform illumination have regions which are poorly illuminated having a dull appearance. Contrast stretching [10] techniques are commonly used to remove the dullness from images. However, to remove the effect of non-uniform illumination, a contrast stretching technique cannot be applied to the entire image as the histogram of such images already spans the entire range of intensity values. A stretch in contrast would brighten the regions having good illumination and darken the regions with poor illumination, degrading the image further. To overcome this problem, the effect of non-uniform illumination is removed using adaptive contrast stretching techniques [10] [36]. An example of such a technique is adaptive histogram equalisation [10]. It is a moving window operation which replaces the center pixel value with the corresponding intensity after a histogram equalisation applied to the pixels within the window. Using a window of the optimum size, one can use this technique to remove the effect of non-uniform illumination. However, the resulting image has an artificial appearance with a 'halo' artifact inroduced around large objects. Hence, an adaptive contrast stretching technique is unsuitable when the target image is to be used for diagnostic purposes. An example of applying histogram equalisation and adaptive histogram equalisation to a sample image is shown in figure 4.1.

Another popular technique to remove the effect of non-uniform illumination is homomorphic filtering [10]. Here, the effect of illumination is modelled as a multiplicative degradation:

$$I = I_0 \times L \tag{4.2.1}$$

where I_0 is the image without illumination degradation, L is the degradation function, and I is the degraded image. To convert the multiplicative effect into an additive effect, logarithm is applied on both sides of the above equation. Assuming L to be a slowing varying phenomenon, its effect is removed by supressing the low frequency content in the obtained log-transformed image. The image with illumination variation supressed is then obained by taking an anti-logarithm. This technique is typically implemented in the frequency domain. However, in the case of Zeiss images, the black boundaries outside the circular aperture will corrupt the spectral information. In order to avoid this, homomorphic filtering needs to be

implemented in the spatial-domain.

An alternative approach to estimate the slowly varying function L is to blur the corrupted image. The blurring operation should blur the corrupted image so as to retain only the illumination variation. Ihe corrected image can be obtained by dividing the corrupted image with this estimate. This obtained result is called the 'Self-Quotient Image' and has been proposed as a robust technique for illumination correction of face images [36] [32] [33].

Though homomorphic filtering and self-quotient image remove the effect of non-uniform illumination, there is no control on the level of illumination (or the brightness) in the resulting image. They commonly have to be followed by brightness and contrast operations in order to achieve an optimum level of illumination and contrast [36]. Moreover, they affect the fidelity of the original image as they reduce the illumination of large and bright objects. This is because, a large bright object will be considered as a region of excessive illumination and will be corrected so as to reduce the illumination. In the case of FFA images, the optic-disc and hemmerhages would be the compromised structures.

Successfull illumination correction of FFA images has been proposed in [5] where a parametric bi-cubic model for the illumination function is proposed. The Parameters are estimated using 25 sample points on the FFA image. These points cannot lie on regions of the retina which are inherently dark (like the macula), or are inherently bright (like the blood vessels). To avoid this, the IC operation is preceded by detection of macula and blood vessels. Another technique which uses the vasculature in retinal images to perform an IC has been proposed in [13]. The assumption here is that the illumination along the prominant vasculature should ideally be uniform throughout the image. However, both the above techniques ([5] and [13]) use the locations of the vessels and/or macula, which is undesirable as stated in Section 4.1.

The effect of illumination can alternatively be modeled as an additive degradation as follows.

$$I = I_0 + L \tag{4.2.2}$$

Here again, L can be estimated in the similar fashion, as in the case of self-quotient image, by blurring the corrupted image. The corrected image can then be obtained by subtracting the blurred image from the original image (The intensity values of obtained result will have to be rescaled to span the standard range of integer values from 0 to 255). However, the resulting image generally suffers from poor brightness and contrast, as in the case of results obtained with self quotient image based technique and homomorphic filtering.

In the next section, we present an improved technique for IC of retinal angiogram images which is based on the self-quotient image technique. It does not involve any parameter setting and has all the charateristics of an ideal IC technique listed in Section 4.1.

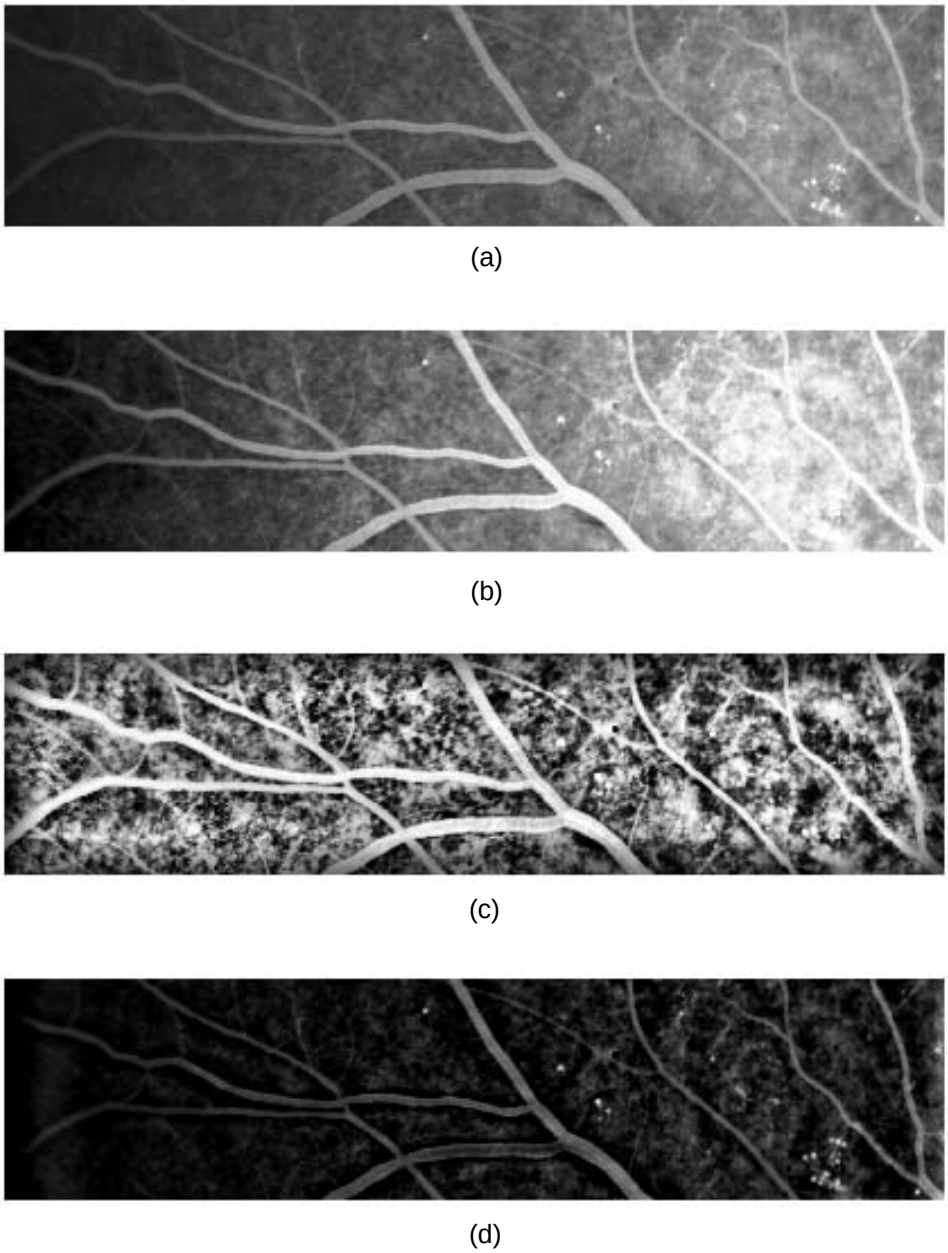

Figure 4.1. Examples of Histogram Equalisation and Homomorphic Filtering. (a) Original Image (b) After Histogram Equalisation (c) After Adaptive Histogram Equalisation with a 25×25 moving window (d) After Homomorphic Filtering

4.3. Modified quotient-image based illumination correction

The technique we propose assumes that the illumination degradation can be modeled as a multiplicative effect (equation 4.2.1). The illumination variation is estimated, as in the case of self-quotient image

based technique, by blurring the corrupted image. However, the degradation function is estimated in a slightly different fashion so as to achieve ideal illumination and optimum contrast.

Let I denote the corrupted-image function, I_s the blurred-image function, I_0 the corrected image function, and L the degradation function. Let the location of a pixel be (x, y) and l_0 be the ideal desired level of illumination. The degradation function is a measure of the degree by which the illumination level at pixel location is lower than the ideal illumination level. Hence, it is estimated as follows.

$$L(x,y) = \begin{cases} \dfrac{I_s(x,y)}{l_0} & \text{if } I_s(x,y) < l_0 \\ 1 & \text{if } I_s(x,y) \geq l_0 \end{cases} \tag{4.3.1}$$

Using the this estimate, the corrected intensity value of a pixel at (x, y) is obtained as:

$$I_0(x,y) = \begin{cases} I(x,y) \times \dfrac{l_0}{I_s(x,y)} & \text{if } I_s(x,y) < l_0 \\ I(x,y) & \text{if } I_s(x,y) \geq l_0 \end{cases} \tag{4.3.2}$$

As can be observed from equation 4.3.2, a pixel where the estimated illumination is greater than the ideal illumination value is not corrected. This ensures that the regions which are inherently bright, like the optic-disk, hemmerhages, etc., are not wrongly classified as regions of excessive illumination and corrected accordingly. When the estimated illumination value is less than the ideal illumination value, scaling by $\dfrac{l_0}{I_s(x,y)}$ ensures that regions with illumination less than the l_0 are elevated to the ideal illumination value. Moreover, contrast at such a pixel is 'improved' by a factor of $\dfrac{l_0}{I_s(x,y)}$. Hence, the propsed IC technique removes the need for subsequent brightness and contrast operations, as required in the case of quotient-image based technique and homomorphic filtering.

4.4. Results and discussion

The proposed technique was implemented using a value of 120 for l_0 (see equations 4.3.1 and 4.3.2). It was selected based on the observation of the well illuminated regions over a number of images. Owing to the large size of the images, the blurring operation was performed on a subsampled version of the original image to achieve faster processing. The images were reduced to one-fourth their dimensions and blurred using a Gaussian-mask of size 30×30. The resulting image was upsampled, one level at a time, while blurring the image using a Gaussian mask of size 5×5 at each upsampled level.

The results of applying the self-quotient image technique, and the proposed technique using the above

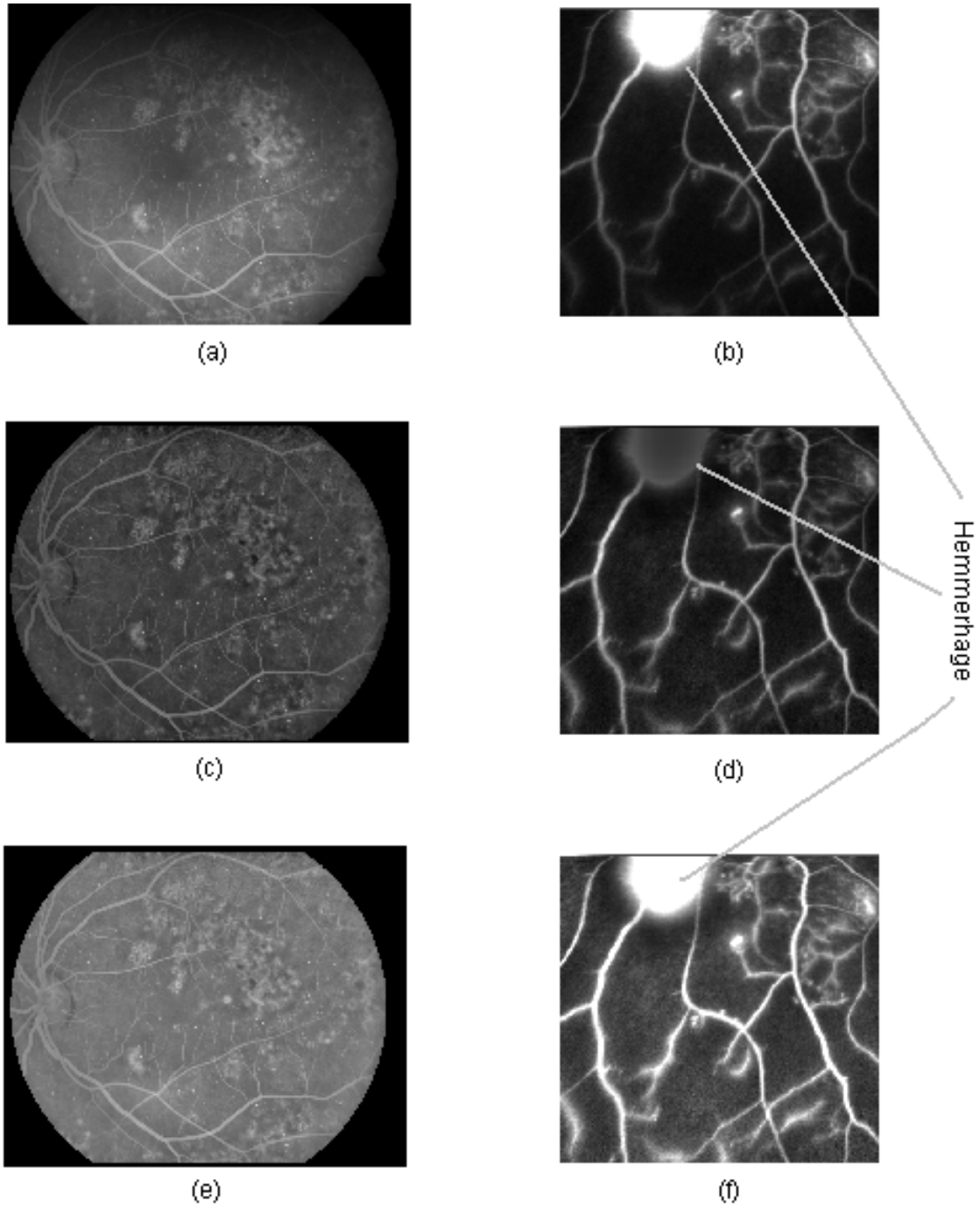

Figure 4.2. Results of applying the self-quotient image technique and the proposed technique. (a) An original Zeiss image. (b) An original HRA image. (c) Zeiss image corrected by self-quotient image technique. (d) HRA image corrected by self-quotient image technique. (e) Zeiss image corrected by the proposed technique. (f) HRA image corrected by the proposed technique.

mentioned parameters, are shown in Figure 4.2. Though the self-quotient image technique removed the

variation in illumination, the images have a dull appearance. Moreover, the intensity of the hemmerhage in the HRA image has been reduced by the self-quotient image technique. Both these drawbacks are absent in the results obtained using the proposed technique.

The value for l_0 and the sizes of the masks for blurring the image are fixed for all images obtained using a particular system (in our implementation, we have used the same set of parameters for Zeiss as well as HRA images). They need not be tuned for every image, and hence, the technique does not need any manual intervention for successfull IC of FFA images. Moreover, it does not use the location of other parts of the retina and does not affect the fidelity of the image. Hence, we can conclude that the proposed technique satisfies all the characteristics of an ideal IC technique listed in Section 4.1.

Though the proposed technique and discussion in this chapter pertained only to FFA images, the techniques can also be applied to illumination correction of colour retinal images. For this, the IC should be performed on the green channel of the colour images, and the corrections should be carried over to the red channel. We do not discuss the IC of colour retinal images in detail as it is beyond the scope of this thesis.

Chapter 5. Detection of Blood Vessels

5.1. Introduction

Every part of the human body requires a healthy supply of blood for proper functioning. Blood is the transport system by which oxygen and nutrients reach the body's cells, and waste materials are carried away. *Lungs* purify the blood by removing the waste materials and through re-oxygenation. Pure and oxygenated blood is pumped to various parts of the body by the *heart*. At one end, blood leaves the heart through large vessels called the *arteries*, and at the other end, it reaches body cells through a network of microscopic vessels called the *capillaries.* Impure blood is carried back to the heart by another set of vessels called the *veins.* The heart, lungs, arteries, veins and the capillaries, together with blood constitute the *circulatory system* of the human body. The arrangement of the blood vessels - arteries, veins and capillaries, is called *vasculature.* In this chapter, we focus our attention on the detection of prominant vasculature from FFA images. We shall use the term 'Blood Vessels' to refer to the prominent vasculature visible in an FFA image.

In general, the health of the retinal vasculature provides a vital cue to the patient's health. Diseases of the retina, like the DR, affect the structure and functionality of the blood vessels in the retina. The degree of change in the structure and functionality directly indicates the extent of the disease. Typically, the vessel calibre [26], tortuosity [31] and 'beadyness' [29] are indicators of the extent of the damage caused by any particular disease.

Information about the blood vessels is also of use for image analysis. It can be hypothesized that regions of CNP (see Section 1.1 and Chapter 7) are bounded on at least one 'side' by prominant vasculature. Hence, an image analysis system designed to detect CNP can use the location of the vasculature to validate the detected regions. Blood vessels can also be used in constructing of retinal montages as they serve as efficient landmarks for image matching [22] [8]. Hence, detection of blood vessels is important for both disease diagnosis as well as computer aided image analysis of FFAs.

5.2. Background and related work

When an FFA image is visualised as a surface in 3D space, blood vessels form topographical ridges. Hence, the problem of blood vessel detection can be formulated as an image analysis problem of ridge detection. Most techniques in literature use such a formulation to detect blood vessels from FFA images. One of the first attempts to detect blood vessels assumes that the ridges (or the blood vessels) have a

Gaussian profile, and detects them using matched filters [30]. The matched filtering is performed using 1D Gaussian templates of length fifteen pixels along six different orientations (twelve different directions). The maximum response from these six filters is thresholded to obtain the blood vessels. Hoover *et al.* [24] modified this technique, using an improved thresholding scheme, to increase the detection rate. However, both these techniques detect the entire thickness of the vessels and not the medial lines. The techniques which detect the entire thickness will have be followed by a another operation to locate the medial lines.

Medial lines are more useful than the entire thickness as they assign a unique location, and define a unique orientation, of the blood vessels. Can *et al.* [26] proposed an automated vessel tracing algorithm to detect the medial lines of blood vessels. The medial lines are traced by traversing along the local orientation. Initial seeds for the tracing procedure are obtained by locating intensity maxima along the horizontal and vertical directions. The orientation of the vessel at a given seed pixel is determined using eight different oriented 1D Gaussian templates, similar to the procedure in [30]. Though this technique can detect a wide range of ridge profiles, the template matching operations for eight different orientations make it computationally expensive.

Apart from the above techniques, the general problem of ridge detection has been approached in the past using geometric properties of image surfaces [12] [19] [27] [9] [18]. To note specifically, curvature of the 'image surface' has been used to detect ridge like features from digital images. Jana and Klein [15] use such an approach, together with morphological techniques, to detect blood vessels in retinal images. Maintz *et al.* [19], Eberly *et al.* [9], and Lopez *et al.* [18] use examples of different ridge profiles to illustrate the superiority of the curvature based techniques for ridge detection over other techniques. The complete scope of these techniques can be determined theoretically and is presented in Appendix D. Because of their superiority, in this chapter we discuss curvature based ridge detection techniques in detail and present a novel technique for the estimation of surface curvature. An algorithm based on this estimate, for the detection of blood vessels at a single scale as well as at multiple scales is also developed.

5.3. Ridge detection from curvature of the image surface.

Curvature based ridge detection techniques are based on the fact that medial lines of ridges are characterised by high magnitudes of curvature along the direction perpendicular to the ridge. A technique using the curvature information will require an efficient algorithm to estimate the surface curvature. Monga *et al.* [21] proposed a computational algorithm based on the differential geomtery of image surfaces to detect ridges. Here, medial lines of ridges are located as the points of directional maxima of the *maximum principle curvature* (MPC) of the image surface [25]. Calculation of MPC requires techniques which estimate the first and second directional derivatives of the image function and is a computationally an expensive operation. In this section, we propose a novel technique for curvature estimation and develop

an algorithm for ridge detection using this estimate. Computationally, this technique is equivalent to the derivative estimation step of the Monga *et al.* algorithm. However, it does not involve any further calculations, unlike in the case of Monga *et al.*'s algorithm where one has to calculate MPC using the estimated derivatives. This makes our algorithm computationally more efficient than the Monga *et al.* algorithm.

5.3.1. Surface Tangent Derivative: A novel ppproach to curvature estimation

The curvature at some point on the image surface (see Appendix A) is a measure of the 'bend' in the surface along a particular direction. Because of this direction specific nature of curvature, one can estimate the curvature along a particular direction by estimating the curvature of the 1D profile of the image intensity values along that direction. In this section, we present a technique for estimation of the surface curvature of 2D digital images using such an approach. Before presenting the technique, we shall first review the definition for curvature of a 1D function.

Let $y = f(x)$ be a 1D function. Let the tangent at a point $P : x$ on this function make an angle θ with the x-axis as shown in Figure 5.1. If dl is the differential arc length at the point P, then the curvature of the function $f(x)$ at this point is defined as:

$$\kappa(x) = \frac{d\theta}{dl} = \frac{d\theta}{\sqrt{dx^2 + dy^2}} = \frac{\frac{d\theta}{dx}}{\sqrt{1 + \left(\frac{dy}{dx}\right)^2}} \tag{5.3.1}$$

Since θ is the angle made by the tangent with the x-axis, it can be computed as:

$$\theta = \tan^{-1}\left(\frac{dy}{dx}\right) \tag{5.3.2}$$

Hence, $\frac{d\theta}{dx}$ can be computed as

$$\frac{d\theta}{dx} = \frac{d}{dx}\left[\tan^{-1}\left(\frac{dy}{dx}\right)\right] = \frac{\frac{d^2y}{dx^2}}{1 + \left(\frac{dy}{dx}\right)^2} \tag{5.3.3}$$

Substituting the above expression in equation 5.3.1, we get:

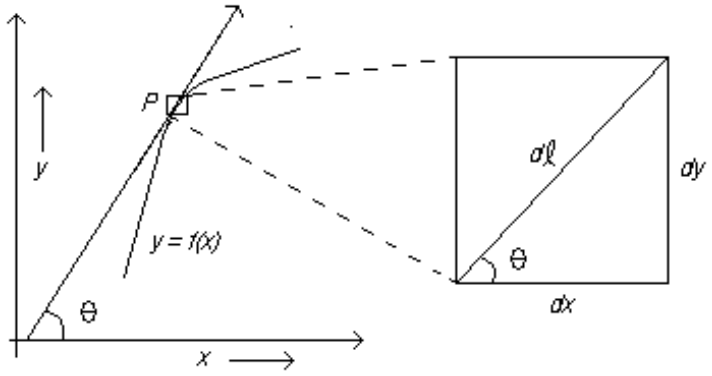

Figure 5.1. Illustration of curvature of a 1D function.

$$\kappa(x) = \frac{\frac{d^2y}{dx^2}}{\left[1 + \left(\frac{dy}{dx}\right)^2\right]^{\frac{3}{2}}} \tag{5.3.4}$$

The feature specificity of the curvature measure can be understood by considering the properties of the derivatives of the profile function at the medial points. According to Haralick [12], medial lines of ridges are loci of points where the second directional-derivative of the image function is a negative minimum (which in other words is to say a magnitude maximum with a negative value). Moreover, the first derivative of the profile function vanishes at the medial points. These two properties are captured simultaneously by the curvature expression in equation 5.3.4. At a medial point, the numerator of this expression attains a magnitude maximum while the denominator attains a magnitude minimum. Hence, the curvature measure will peak sharply at the medial points of ridge profiles.

The expression for $\frac{d\theta}{dx}$ in equation 5.3.3 will also peak sharply at the medial points of ridge profiles for the same reasons as mentioned above. However, because of the lower power of the denominator in this expression, the feature specificity of this measure will be slightly lower as compared to that of the curvature measure. However, for most image processing/analysis applications, an accurate evaluation of the curvature is not neccessary and an estimate which directly follows the correct value of curvature is sufficient. To detect ridges for example, it is enough if an estimate is approximately as feature specific as the curvature measure. Hence, the technique we propose calculates the value of $\frac{d\theta}{dx}$ as an estimate of the curvature measure and not $\frac{d\theta}{dl}$. As we shall see later in this section, this expression lends itself for a simple and a computationally efficient implementation.

$\frac{d\theta}{dx}$ is the derivative of the angle made by a tangent with the x-axis. In the case of 2D images, this corresponds to a derivative of the angle made by a surface tangent line with the base-plane, in some direction. Since our estimate is not the true curvature, and since it is the derivative of the angle made by a tangent, we call it as the **Surface Tangent Derivative** (STD). At any given point on the surface, an STD measure can be obtained for every possible direction, measuring the bend in the surface along that particular direction. However, for a function defined over a discrete grid (as is the case with 2D digital images), it is possible to evaluate the STD measure only along a finite number of directions. In general, it is sufficient if the a curvature measure is obtained for the four different directions corresponding to the 8 neighbours of a pixel. These four directions are specified in the set $\Omega = \left\{ -45^\circ, 0^\circ, 45^\circ, 90^\circ \right\}$ (see equation C.1 in Appendix C).

The proposed scheme calculates the STD measure using mask operations on the image intensities. Incorporating the mask size and direction information into the notation, the STD measure at a pixel location (n, m), along a direction α, estimated using a mask of size $n \times n$, is denoted by $\underset{\alpha}{\overset{n}{K}}(n, m)$ in the rest of this thesis.

Using equation 5.3.3, the angle made by the surface tangent with the base-plane at a pixel (n, m), along the direction α in the base-plane, is calculated as:

$$\underset{\alpha}{\Psi}(n, m) = \tan^{-1}\left[\underset{\alpha}{G}(n, m) \right] \tag{5.3.5}$$

where $\underset{\alpha}{G}(n, m)$ is the first directional-derivative (gradient) of the image function along the direction α in the base-plane. This is calculated using the generalised Sobel masks (Appendix C) as follows:

$$\underset{\alpha}{G}(n, m) = \frac{\sum_{i=-w}^{w} \sum_{j=-w}^{w} \left\{ \underset{\alpha}{\overset{N}{M}}(j, i)\, I(n + j, m + i) \right\}}{\sigma_N} \tag{5.3.6}$$

where $N \times N$ is the size of the generalised Sobel mask, $w = \frac{N-1}{2}$, and σ_N is the sum of the positive elements of the mask $\underset{\alpha}{\overset{N}{M}}$. The STD value is nothing but the derivative of the angle $\underset{\alpha}{\Psi}$ which can be calculated as follows:

$$\underset{\alpha}{\overset{N}{K}}(n, m) = \frac{\sum_{i=-k}^{k} \sum_{j=-k}^{k} \left\{ \underset{\alpha}{\overset{2k+1}{M}}(j, i)\, \underset{\alpha}{\Psi}(n + j, m + i) \right\}}{\sigma_{2k+1}} \tag{5.3.7}$$

The directional-derivative is equation 5.3.7 is calculated using a mask of size $(2k + 1) \times (2k + 1)$. Since the derivative in equation 5.3.6 can be performed using a mask of variable length, once can keep the value of k fixed and achieve the desired amount noise filtering by choosing an appropriate value for N.

Hence, the overall operation to calculate STD can be considered to involve only one parameter N. For ease of reference, this parameter is called as the 'mask size' for calculating STD.

Next we show how STD can be used to perform ridge detection.

5.3.2. Ridge detection using STD

The curvature measure at a ridge pixel is a maximum in some direction. Hence, ridges can be detected by locating pixels where the magnitude of STD is a maximum along some direction. The magnitude of STD at a ridge pixel is the strength or measure of ridge-ness at that pixel. Local magnitude maxima of STD can also occur at locations of valley pixels. However, a ridge is characterised by negative values of STD, while a valley is characterised by positive values of STD. The complete algorithm for ridge detection is as follows.

Ridge Detection Algorithm

Let $I(n, m)$ be the image function. Calculate the STD for four different directions as $\underset{\alpha}{\overset{N}{\mathrm{K}}}(n, m)$, $\alpha \in \Omega$ (equation C.1) with a mask of size N as in equation 5.3.6. Let t_K be the threshold for ridge strength. For every pixel location (n, m), do the following:

1. *Evaluate* $\left| \mathrm{K}_{\max} \right| = \max\left\{ \left| \underset{\alpha}{\overset{N}{\mathrm{K}}} \right| \;\middle|\; \alpha \in \Omega \right\}$ *and the corresponding orientation* $\alpha_{\max}$.

2. *If* $\left| \mathrm{K}_{\max} \right| > t_K$ *and* $\underset{\alpha_{\max}}{\overset{N}{\mathrm{K}}}(n, m) < 0$, *then:*

   i. *Check if* $\left| \mathrm{K}_{\max} \right|$ *is greater than* $\left| \underset{\alpha_{\max}}{\overset{N}{\mathrm{K}}} \right|$ *of the neighbouring pixels corresponding to the direction* $\alpha_{\max}$. *If yes, then mark the pixel* (n, m) *as a ridge pixel. Else, do nothing.*

   For example, if $\alpha_{\max} = -45^{\circ}$, *then check if*

$$\left| \mathrm{K}_{\max} \right| > \left| \underset{\alpha_{\max}}{\overset{N}{\mathrm{K}}}(n-1, m+1) \right|$$

and

$$\left| \mathrm{K}_{\max} \right| > \left| \underset{\alpha_{\max}}{\overset{N}{\mathrm{K}}}(n+1, m-1) \right|$$

   If yes, then mark the pixel (n, m) *as a ridge pixel. Else, do nothing.*

Else: Do nothing.

By selecting the right value of the threshold t_K, one can put a lower limit on the strength of the detected ridges. This threshold also ensures that noise does not wrongly classify non-ridge pixels as ridge pixels. In order to obtain better continuity in the detected ridge lines, one can use two different threshold values and perform *hysteresis thresholding* [3]. For ease of reference, the mask width N, used to calculate the STD values, will be called as mask size of the blood vessel detection algorithm.

5.3.3. Multiscale ridge detection

In practice, it can be observed that blood vessels occur with varying cross-sectional widths. Hence, applying the algorithm proposed in the previous section with a fixed mask size will be unable to detect *all* ridges (of different widths). In order to detect vessels with different widths, the algorithm should be applied repeatedly, using masks of different sizes, and the obtained results should be collated to obtain the final result. In this section, we present an efficient scheme for such a collation operation.

The collation scheme is based on the fact that in an FFA image, thin vessels branch out of thicker vessels. When the ridge detection algorithm is applied with a small mask, these vessels are detected along with many other noisy structures. However, when a larger mask is used to detect ridges, noise is suppressed and only thick vessels are detected. Using these observations, the collation scheme can be formulated as follows.

Multiscale Collation Scheme

Let λ_n denote the set of ridge pixels detected using a mask of size $n \times n$. Let Λ be the complete set of ridge pixels after collation of results obtained using different mask sizes. Let $\lambda_{n_1}, \lambda_{n_2}, \ldots, \lambda_{n_k}$ be the ridge pixels obtained with different mask sizes such that $n_1 < n_2 < \ldots < n_k$. Then, Λ is obtained as follows.

1. $\Lambda = \lambda_{n_k}$
2. *For $i = k - 1$ to 1, do the following.*
   - *i.* $\Lambda = \Lambda \cup \nu$, *where ν is the set of pixels in λ_{n_i} 8-connected to at least one pixel in Λ.*
   - *ii. Repeat step (i) until no further pixel is added to Λ.*

The requirement for multiscale detection of ridges is independent of underlying single scale ridge detection scheme. Ridges will *have* to be detected at multiple scales if one is desirous of detecting vessels of all possible cross-sectional widths. The above technique collates medial lines of ridges obtained at different scales and does not make use of the curvature measure. Hence, it can also be applied to results obtained using other techniques of ridge detection which do not depend on the curvature measure.

5.4. Results and discussion

The proposed ridge detection algorithm and collation scheme were applied on a test image using the STD values calculated along four directions specified in the set $\Omega = \left\{ -45^{\circ}, 0^{\circ}, 45^{\circ}, 90^{\circ} \right\}$ (see equation C.1). The value of k in equation 5.3.7 was fixed at 1. The ridge detection was performed using masks of sizes varying from 5×5 to 11×11. The obtained results were collated using the proposed collation scheme. The results with masks of sizes 5×5 and 11×11, and the result after collation are shown in Figures 5.2 to 5.5. These figures illustrate the effect of the mask size on the quality of the results. For instance, when ridges are detected using a mask of size 5×5, many noisy structures are also detected along with the blood vessels (Figure 5.3). On the other hand, when ridges are detected using a mask of size 11×11, the thin ridges/blood vessels are not detected (Figure 5.4). However, the problems of noise and missing out thin vessels is solved by using the multiscale collation scheme as seen in Figure 5.5.

Though the scheme proposed in Section 5.3.3 can perform efficient collation, it misses out few of the thin blood vessels. This happens because, the collation scheme only accumulates thin vessels which are connected to the vessels detected using the largest mask. Hence, thin vessels for which the branching point from thicker vessels is not present in the image, are not accumulated. This can be observed in Figure 5.5.

The proposed ridge detection algorithm requires calculation of STD along four directions. Calculation of STD along a direction in turn involves of calculation of two directional derivatives. Hence, calculation of STD is computationally equivalent to calculation of a second directional-derivative. Monga *et al.'s* algorithm also requires calculation of second directional-derivatives [21]. However, their algorithm requires a further calculation of the maximum principle curvature using these directional-derivates. As the proposed ridge detection algorithm does not involve any calculations beyond the calculation of the STD, it is computationally superior to the Monga *et al.* algorithm.

The presentation in this chapter pertained to detection of blood vessels from FFA images. Since blood vessels can be modeled as topographic ridges, ridge detection algorithms was formulated. By making suitable changes, the scope of these algorithms can be extended to detection of valleys/trenches from digital images.

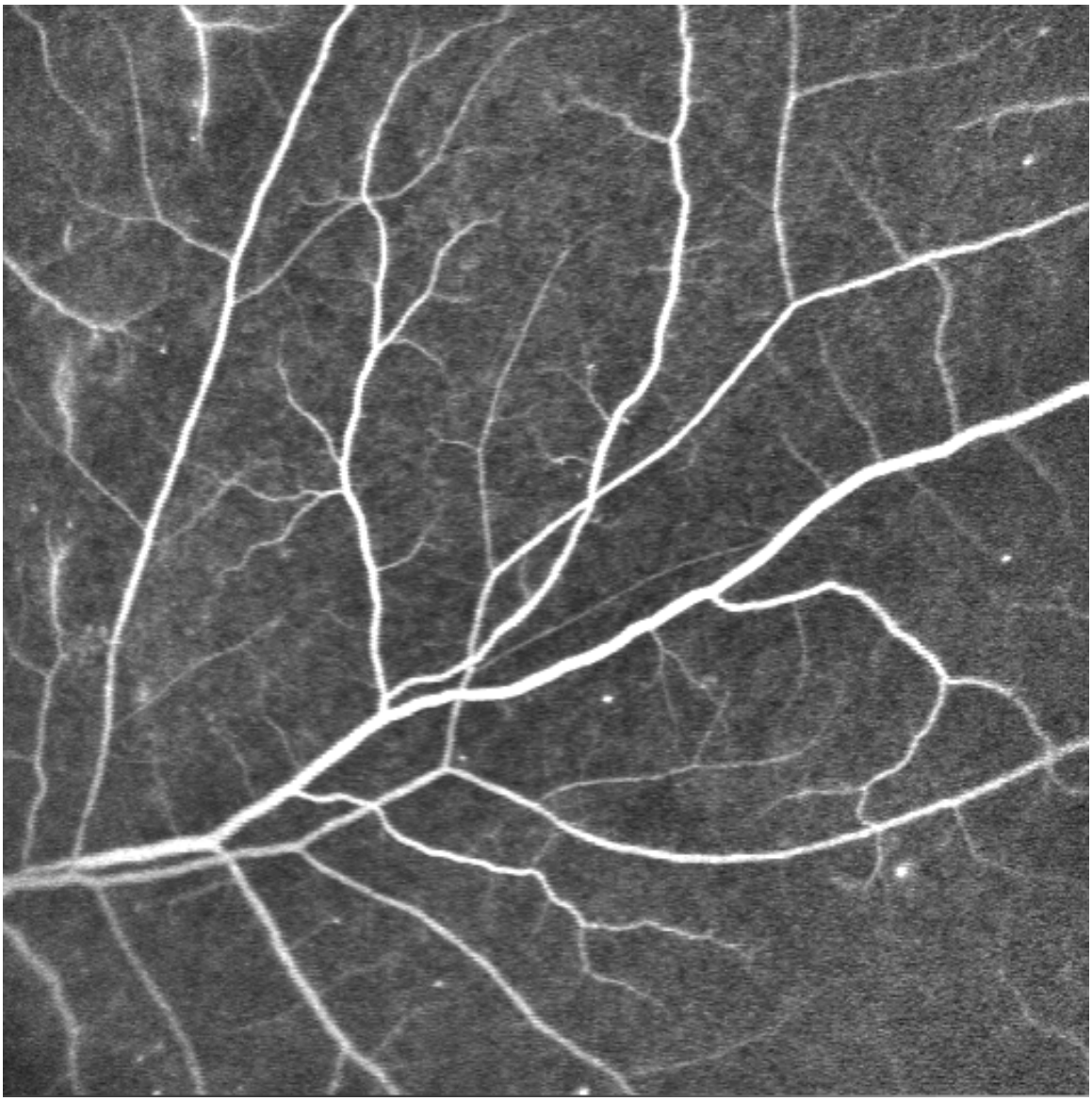

Figure 5.2. An FFA test image.

5.5. Summary

Blood vessel detection is a function of the retinal struture analysis module of the framework proposed in Chapter 3. In this chapter, detection of blood vessels from FFA images was addressed by formulating the problem as a problem of ridge detection from 2D digital images. Because of their superiority over other techniques, curvature based ridge detection techniques were used to detect blood vessels. Techniques using the curvature measure will require an estimate of the curvature value. A novel curvature estimation technique was proposed, using which a ridge detection detection algorithm was developed. Detection of

Figure 5.3. Result of detecting ridges in the test image using a mask of size 5×5.

ridges at a single scale cannot detect blood vessels of all cross-sectional widths. Hence, a novel scheme was proposed, using which vessels detected at different scales can be collated efficiently.

Figure 5.4. Result of detecting ridges in the test image using a mask of size 11×11.

Figure 5.5. Result of detecting ridges in the test image using masks of sizes from 5×5 to 11×11 and collating the results using the proposed scheme.

Chapter 6. Detection of Microaneurysms

6.1. Introduction

Most diseases of the retina alter the structure and the functionality of the vasculature in the retina. One such disease, the Diabetic Retinopathy (DR), leads to the occurance of *capillary non-perfusion* (CNP) and *neo-vascularisation.* CNP is a disease due to which the capillary network in parts of the retina 'drops out' and stops supplying blood. Neo-vascularisation on the other hand, is the growth of new blood vessels branching out of the existing vessels. The early 'sprouts' of these new vessels are called **microaneurysms** (MA). They are bulb-like microscopic structures occuring as small and bright circular disks in FFA images. A microscopic image of MAs, and an FFA image with MAs are shown in Figure 6.1.

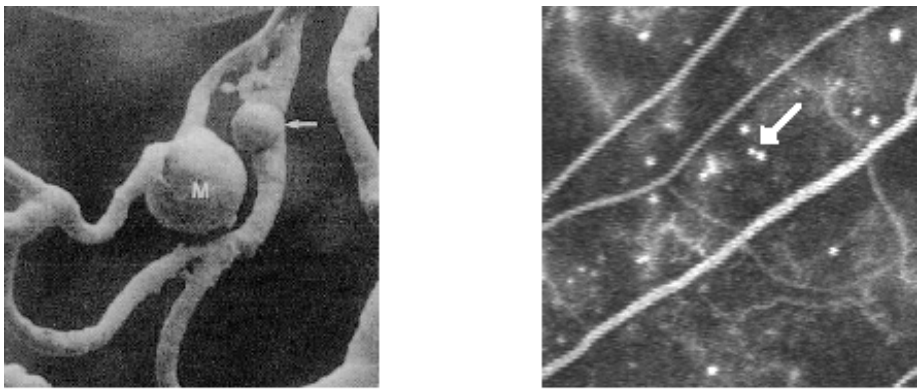

Figure 6.1. (a) A microscopic image of MAs. The larger of the MAs is marked by the letter M, while the smaller one is indicated by an arrow. (b) An FFA image with MAs. Few of the MAs are indicated by an arrow.

The number of MAs in the retina is considered to be an indicator of the extent of damage done by DR. Owing to the large size of FFA images, and to the huge number of MAs occuring in a typical patient with DR, it is not possible for a human expert to get an accurate and complete count of MAs. However, this problem can be solved by using computer aided analysis of FFA images. In this chapter, we present such an analysis technique for detection of MAs from FFA images. Detection of MAs is a function of the disease analysis module of the framework proposed in Chapter 3.

6.2. Background

Most MA detection techniques in literature start by performing pre-processing and retinal structure analysis operations. Pre-processing is either used for illumination correction, or for feature (which are MAs for our current discussion) enhancement. Retinal structure analysis is commonly used in an MA detection system for detection and supression of blood vessels in order to avoid misclassification of a vessel pixel as an MA pixel.

Regions of MAs exhibit many properties. A general procedure to detect MAs makes use of these properties in two steps as shown in Figure 6.2. These steps are:

1. Candidate regions are detected using one of the properties of MAs.
2. The candidate regions are then classified as MA or non-MA using another set of properties of MAs.

With respest to the framework proposed in Chapter 3, step 1 is a function performed by the disease analysis module, and step 2 performed by classification module.

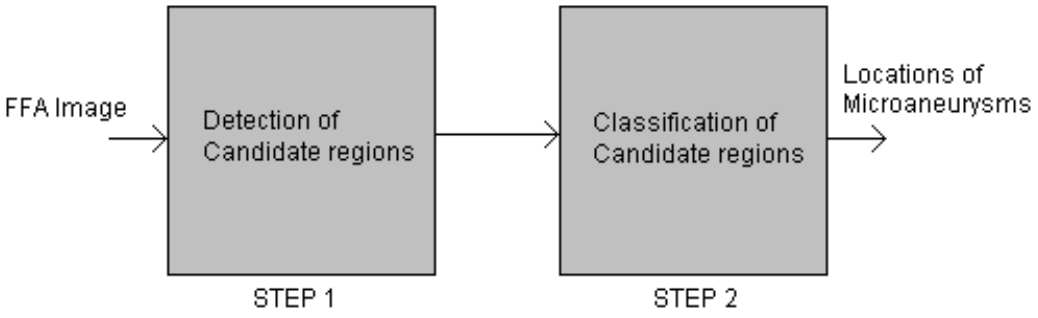

Figure 6.2. The two stage procedure to detect microaneurysms

Spencer *et al.* [28] and Cree *et al.* [4] use the fact that the intensity profile of MAs can be modeled as a 2D Gaussian function to detect the candidate MAs. Accordingly, a matched filtering operation is performed on an FFA image using a Gaussian template. The filtered image is thresholded to obtain all the candidate MA regions. Mendonca *et al.* [20] detect the candidate MA pixels by locating the local intensity maxima. The candidate MA regions are then obtained by a region growing operation at these locations. These are classified using measures such as the area, perimeter, aspect ratio, circularity, gray value statistics, etc., of the candidate regions.

Azeem *et al.* [2], and Hafeez and Azeem [11] use a different approach to detect candidate MAs. They first detect the edges in FFA images using a Canny [3] edge detector. Then, the edges of blood vessels are rejected using the length of the edge as a constraint. The gradients along the remaining edges are further

thresholded to retain only the strong edges. Since MAs are circular disk-like structures, Azeem *et al.* [2] use the circular Hough transform to classify the obtained strong edges. To avoid the high computational cost involved in the computation of the Hough transform, Hafeez and Azeem used measures like the aspect ratio, perimeter, total energy, mean energy etc., for similar classification [11].

In the next section, we present a novel technique for detection of MAs as part of the first block of the Figure 6.2. This technique has a strong theoretical grounding unlike the other techniques in literature which are based on heuristics. A classification of the detected candidate MAs is not presented. However, any technique from one of the above references should serve as a good classifier.

6.3. Detection of microaneurysms from curvature of the image surface

When an FFA image is visualised as a surface in 3D space, MAs form hill like topographical features. Hence, a hill detection algorithm can also detect MAs. In this Section, we present a hill detection algorithm which uses curvature of the image surface to detect MAs (details of image surface can be found in Appendix A and Section 5.3). A typical cross-sectional profile of a hill like feature along some direction, is shown in Figure 6.3. The medial point of such a profile is also called as a 'hill point' or a 'hill pixel'. In Chapter 5, we have seen that medial lines of blood vessels are characterised by maximum curvature along a direction perpendicular to the orientation of vessel. Hill points are characterised by maximum curvature along *all* directions.

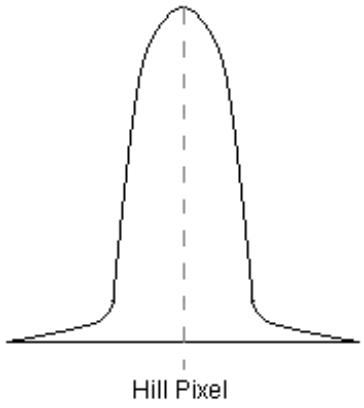

Figure 6.3. Typical cross-sectional profile of a hill like feature.

The algorithm we present detects local maxima of the curvature estimate STD, presented in Section 5.3.1. We shall use the same notation $\underset{\alpha}{\overset{N}{\mathrm{K}}}(n,m)$ to denote the STD measure at a pixel (n,m), along the direction α, calculated using a Sobel mask of size $N \times N$ (see Appendix C and Section 5.3.1 for details).

The hill detection algorithm is as follows.

Hill Detection Algorithm

Let $I(n, m)$ be the image function. Calculate the STD for the four different orientations $\alpha \in \Omega$ (equation C.1) as $\overset{N}{\underset{\alpha}{\mathrm{K}}}(n, m)$ with a mask of size N using equation 5.3.7. Let $t_{\mathrm{K}} > 0$ be the threshold for the curvature strength at the hill pixel. For every pixel location (n, m), do the following:

1. *Initialise a Boolean variable isHill =* **true**.
2. *For each $\alpha \in \Omega$, do the following while updating the variable isHill accordingly.*
    i. *Check if $\overset{N}{\underset{\alpha}{\mathrm{K}}}(n, m)$ is greater in magnitude than the $\overset{N}{\underset{\alpha}{\mathrm{K}}}$ values of its two neighbours along the direction α, and greater in magnitude than t_{K}. If yes, do nothing. If no, then update the value of the variable isHill as isHill =* **false**.
3. *If isHill =* **true**, *then mark the pixel (n, m) as a hill pixel. Else, do nothing.*

The above algorithm uses a threshold t_{K} for the strength of the 'hillness' of a pixel so that the hills detected have a certain minimum strength. This helps in filtering out noise pixels which are otherwise prone to detection as hill pixels. For ease of reference, the width N of the mask used for calculating the STD values will be called as the mask size of the MA detection algorithm.

6.4. Results and discussion

Though MAs are small structures, they can occur in various sizes. In order to detect MAs of all sizes, one has to perform MA detection at different scales and combine the results obtained at each scale. However, the collation of results from different scales is a simple accumulation task and does not require any special care/scheme as in the case of detection of blood vessels (see Chapter 5). Detection at different scales, using the algorithm presented in Section 6.3, can be done by using masks of different sizes. Most FFA images are corrupted by noise. Hence, a mild noise filtering of the images may need to be done before applying the MA detection algorithm.

In the implementation of the proposed algorithm a threshold value of $t_{\mathrm{K}} = 0.95\pi$ was used. This value is the minimum allowed change in the surface tangent angle at a medial point. The STD values were calculated using a fixed value of 1 for the variable k in equation 5.3.7. The initial noise filtering was done using a Gaussian filter with mask size 3×3 and a standard deviation 2. The original image and the corresponding filtered image are shown in Figures 6.4 and 6.5, respectively. The results of applying the

MA detection algorithm with mask sizes 5×5 and 9×9 are shown in Figures 6.6 and 6.7, respectively (the detected MAs are marked by a cross). As expected, the detection algorithm misses the larger MAs in the image when a 5×5 mask is used. On the other hand, when the detection algorithm is applied with a 9×9 mask, only the large MAs in the image are detected. Hence, to overcome this problem, one has to collate the results obtained at multiple scales. This can be seen in the collated result, obtained by collating the results of MA detection with masks of sizes from 5×5 to 9×9, in Figure 6.8.

The proposed algorithm was applied on 62 HRA images and 20 Zeiss images and was found to yield good results. Because of the high number of MAs in a given image, the obtained results were validated visually by retina experts. Hence, we can conclude that the proposed algorithm is a good technqiue for detection of candidate MAs. However, as can be seen in Figure 6.6, there are a few vessel pixels which are wrongly classified as MA pixels. Hence, the algorithm has to be followed by a classification algorithm to weed out the false detections.

6.5. Summary

Microaneurysms are early sprouts of new blood vessels in the retina and occur as tiny disk like structures in an FFA image. Detection of MAs is a function of the disease analysis module of the framework proposed in Chapter 3. In this chapter, a novel curvature based technique for detection of MAs was proposed by modelling them as topographic hills. The MA pixels were located at points where the curvature value was a maximum in *all* directions. Such a technique has a theoretically strong grounding in comparison to other techniques in literature which are based on heuristics. The proposed algorithm was found to yield good results in the sense that all MAs in an image were detected. The results were visually validated by retina experts.

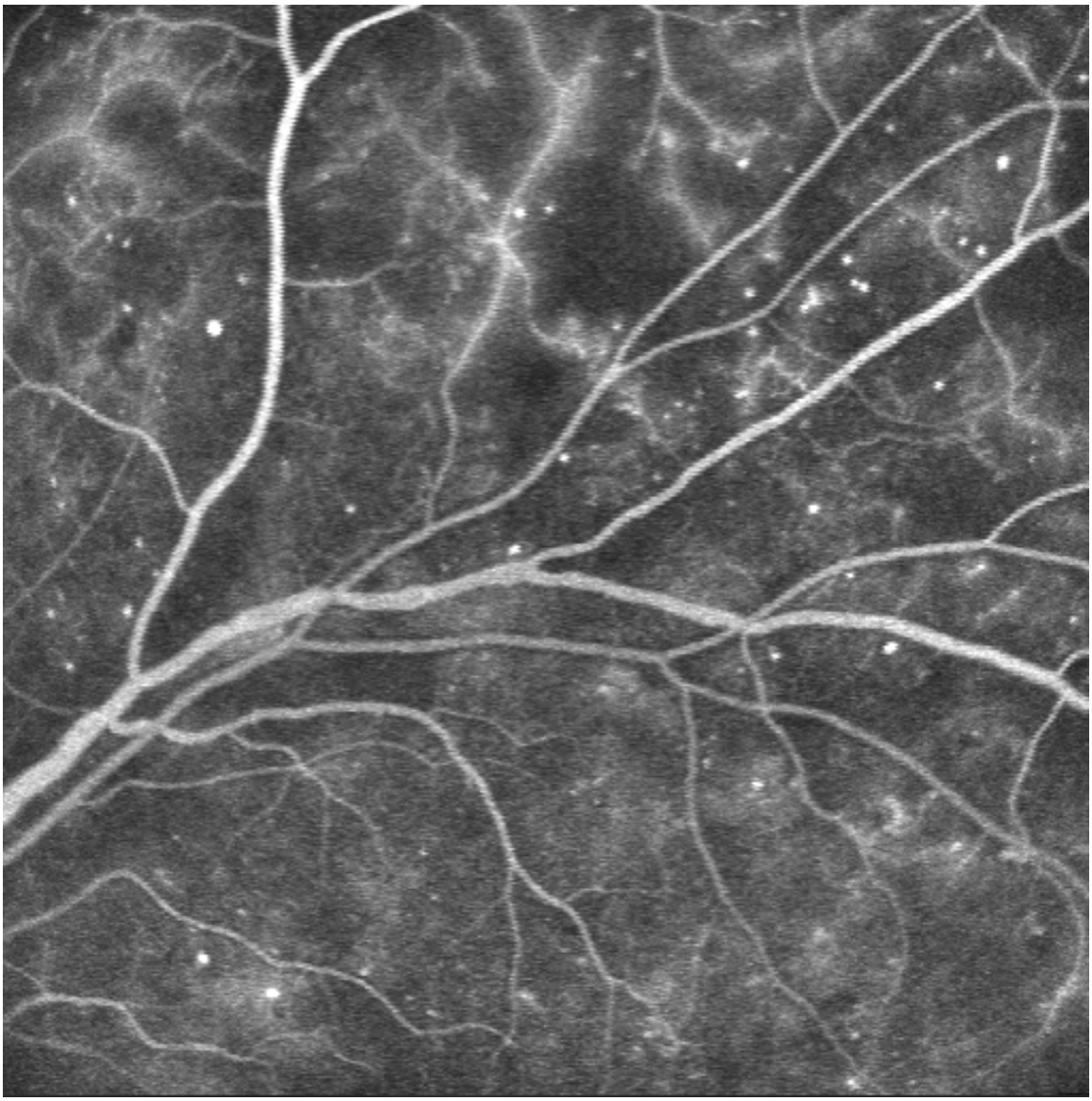

Figure 6.4. An FFA test image.

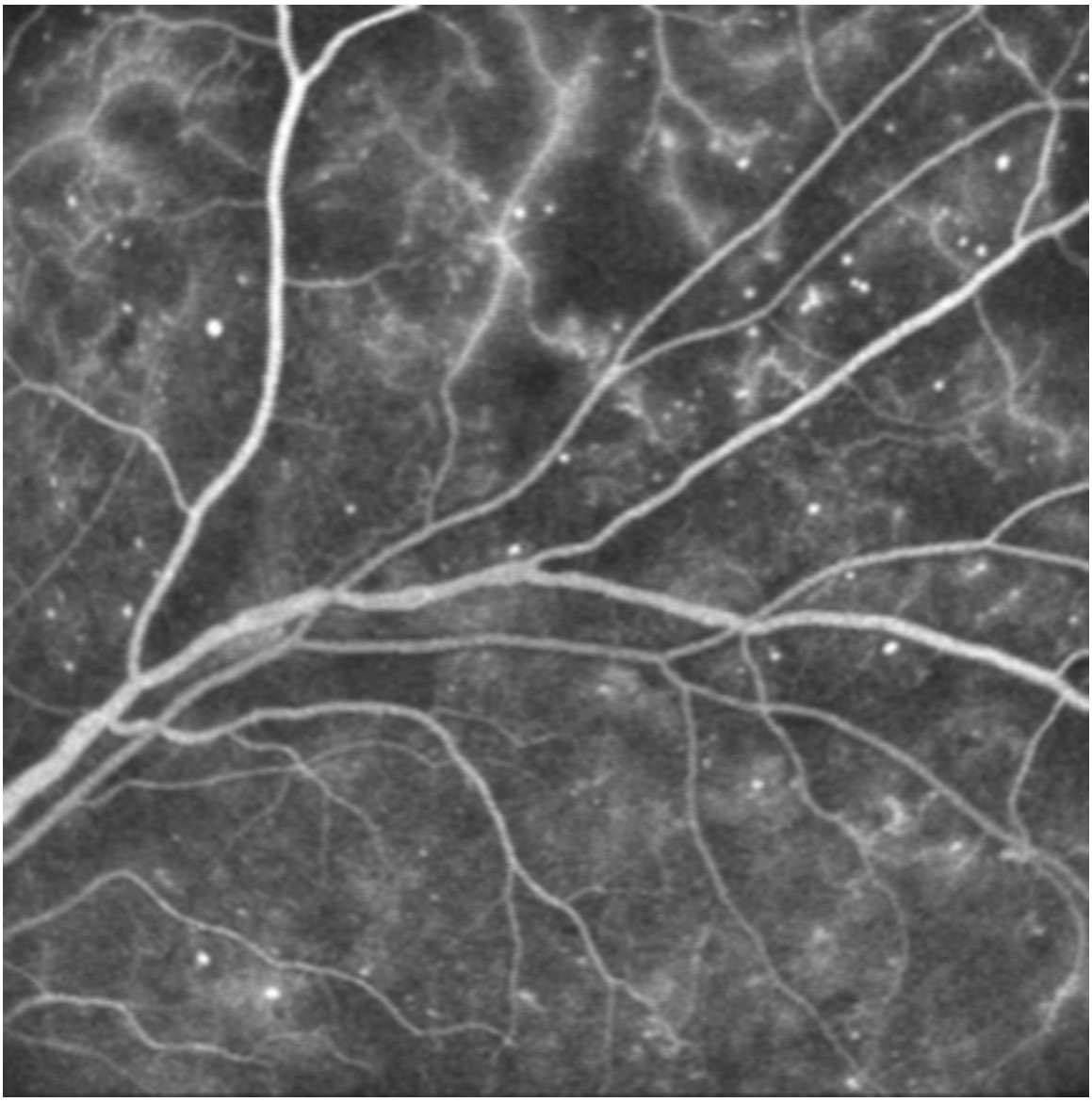

Figure 6.5. Results of applying a Gaussian filter with mask of size 3×3 and a standard deviation 2.

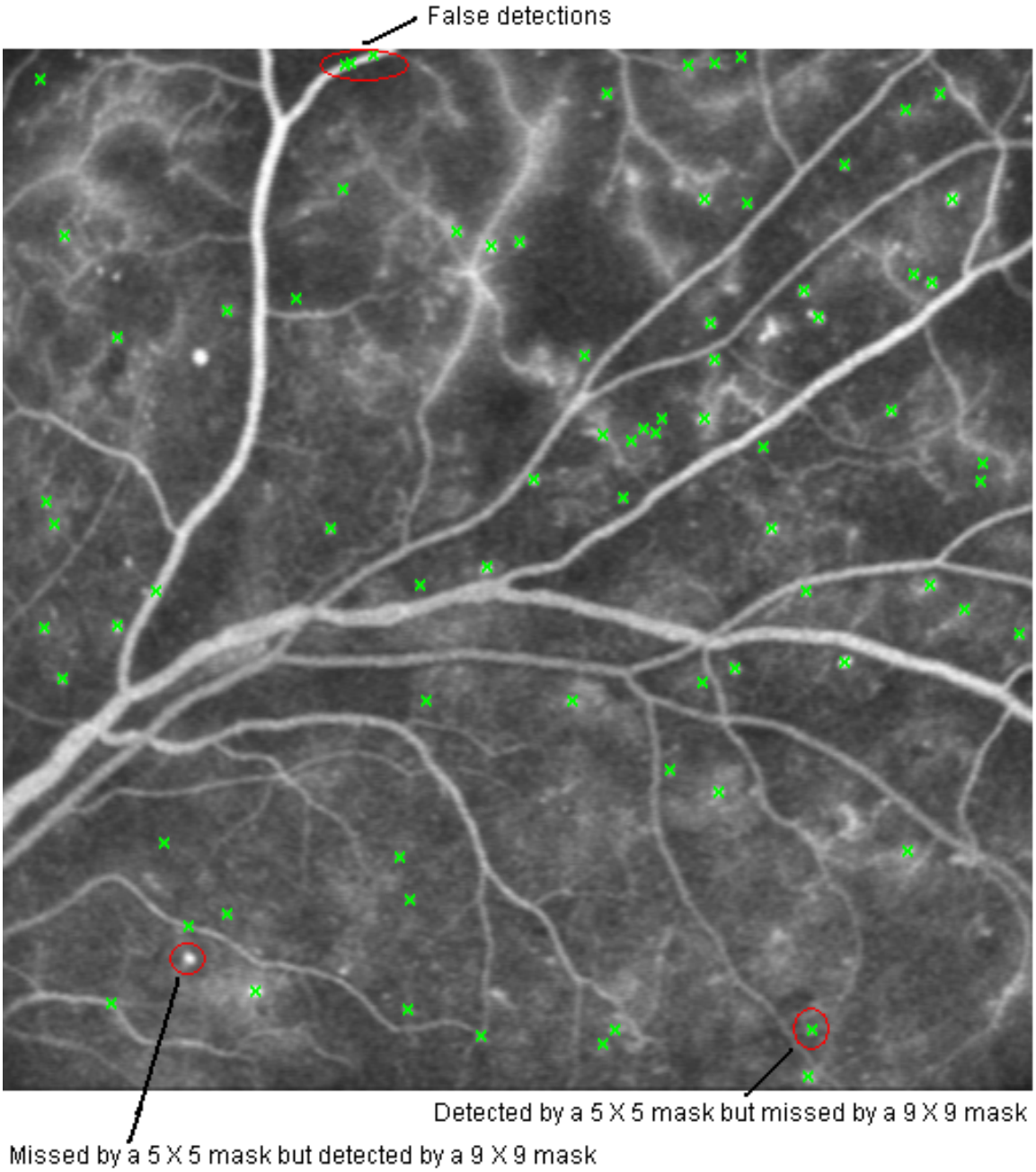

Figure 6.6. MA detection using a mask of size 5×5.

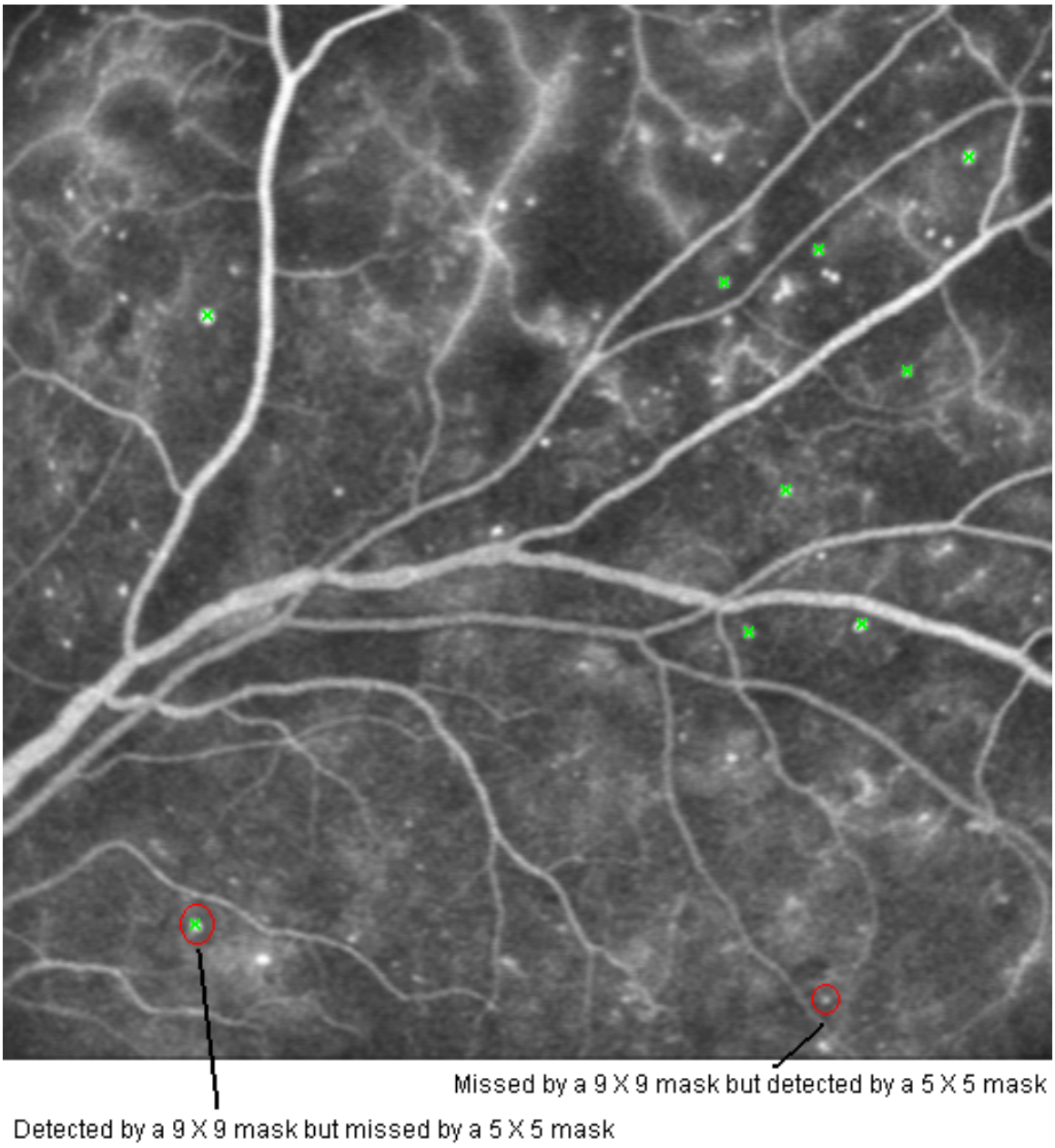

Figure 6.7. MA detection using a mask of size 9×9.

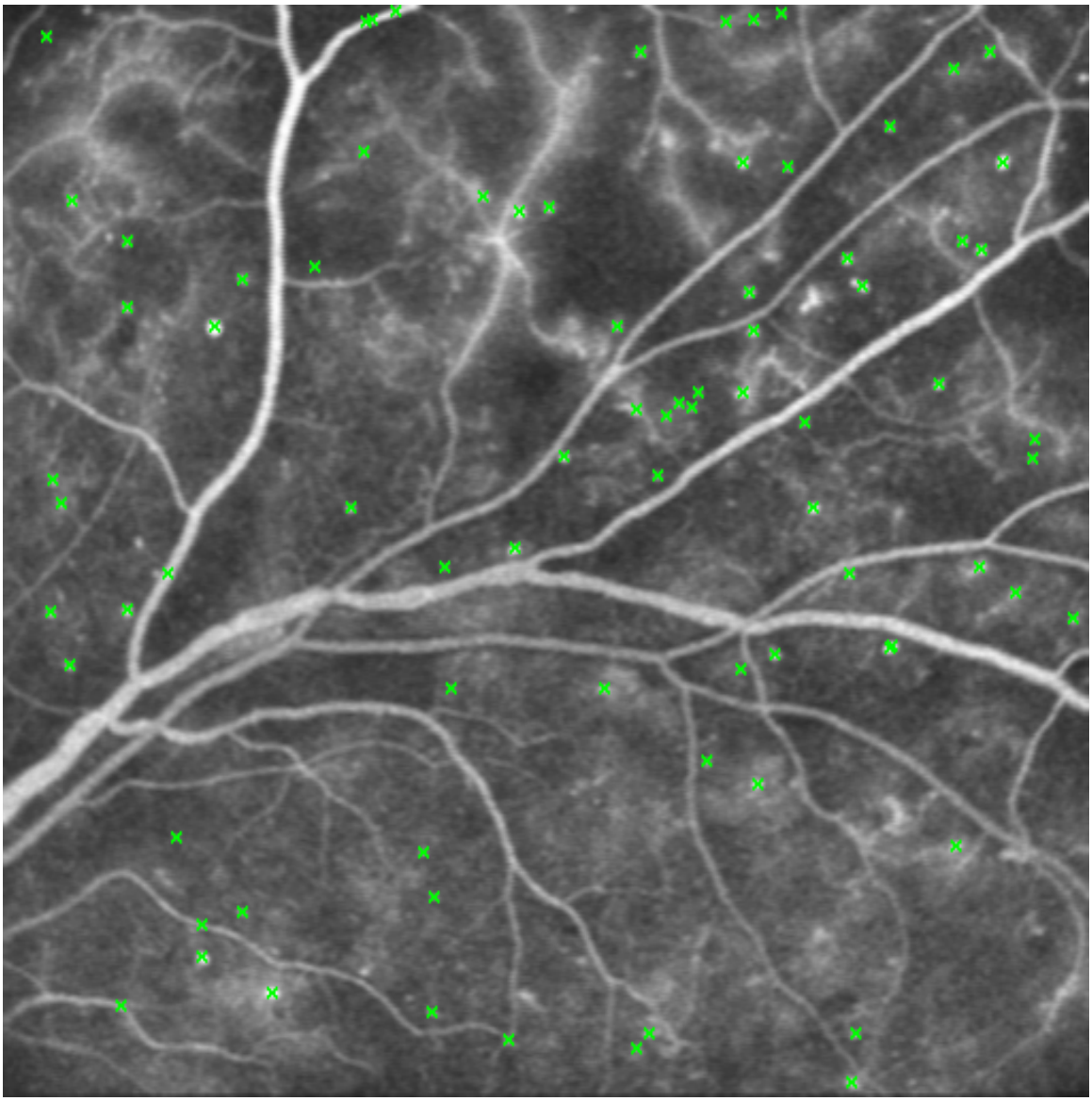

Figure 6.8. Collation of results of MA detection obtained using mask of sizes from 5×5 to 9×9.

Chapter 7. Segmentation of Regions of CNP

In this chapter, we present a technique for extracting regions of *Capillary Non-Perfusion* (CNP) from HRA images. The technique exploits a special property of the HRA images and takes a novel approach to image segmentation. Before we present the technique, we begin with a brief description of regions of CNP and discuss the importance of their detection from FFA images.

7.1. Capillary non-perfusion

Capillaries are microscopic vessels which supply blood to the body tissue. The act of pumping of blood into the body cells by the capillaries is called *perfusion.* **Capillary Non-Perfusion** (CNP) is a disease wherein the capillary network in a region of the human retina (see Chapter 2) stops perfusing blood. CNP can occur due to various reasons but most commonly due to diabetes. If not treated in time, such diseased regions can grow and spread across the entire retina. When such a growth enters the central part of the retina, which is responsible for most of the human vision (see Chapter 2), it can lead to blindness.

The clinical procedure to detect CNP is a visual scan of an FFA image to estimate the amount of area damaged. However, such a procedure suffers from subjectivity and is sensitive to the quality of the images obtained. A computer based analysis system can remove such drawbacks and assign an objective measure to the extent of the disease using well defined quantification procedures. In this chapter, we present a technique to extract and quantify regions of CNP from HRA images using computer aided image analysis. To our knowledge, there is no work reported in literature which addresses this problem.

7.2. Properties of HRA FFA images

The laser camera of the HRA system can penetrate through the retinal layer and capture the capillary network of the choroidal layer. Consequently, one can observe a fine-grain wooly texture, similar to the healthy capillary network, even in regions of CNP. However, due to lack of flourescence in those regions, they appear much darker than the healthy capillary network.

A small part of an FFA image, and its intensity profile along a horizontal line, are shown in Figure 7.1. As can be observed, the prominent vasculature in the image become ‘hills’, and the rest of the areas become bumpy ‘valleys’ or ‘plains’, of the intensity profile. Hence, one can conclude that the prominent vasculature are devoid of local intensity minima unlike the rest of the regions. Furthermore,

it can be concluded that the prominent vasculature is devoid of any local extrema except on the medial points which are maximum points. The reasons for the presence of extrema are the fine retinal capillary network in healthy regions, and the choroidal capillary network in the CNP regions (see Sections 2.1, 2.2, 2.4 for more details). This property of HRA images is illustrated in Figures 7.1 and 7.2 where sub-parts of FFA images and their extrema maps are shown. As expected, the blood vessels are lacking in extrema except on their medial axes.

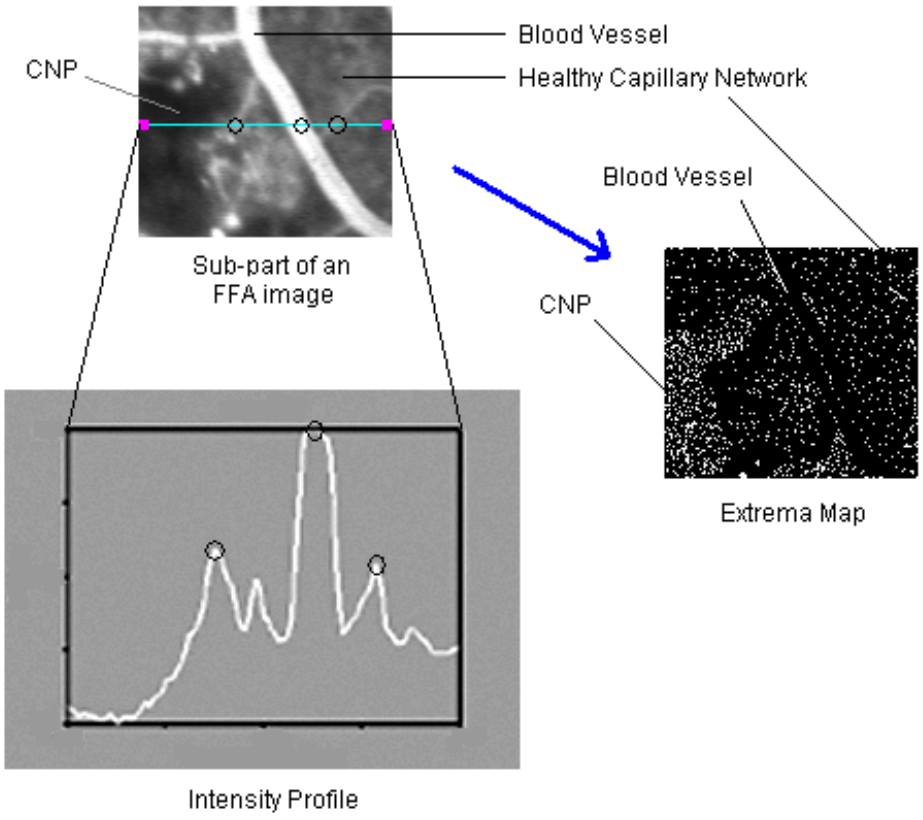

Figure 7.1. Intensity profile of a sub-part of an FFA image and the corresponding extrema map. The prominent peaks in the intensity profile are marked by circles. The white pixels in the extrema map correspond to the extremum pixels. The extrema map clearly illustrates higher density of extrema in the regions of CNP.

As mentioned in Chapter 2, the injected flourescene dye effuses out on to the retinal surface over time and clouds the neighbouring regions. Regions of CNP do not receive the blood that carries the dye, and hence are not clouded. In FFA images, the clouding of retinal regions is equivalent to smoothening of such regions. Smoothening causes a reduction in the density of extrema in the corresponding region. Hence, regions of CNP have a higher density of extrema as compared to regions with a healthy capillary network. An illustrative example, showing such a difference in density of extrema, is shown in Figure 7.3. The difference can also be observed in the sub-part shown in Figure 7.1. In general, the difference

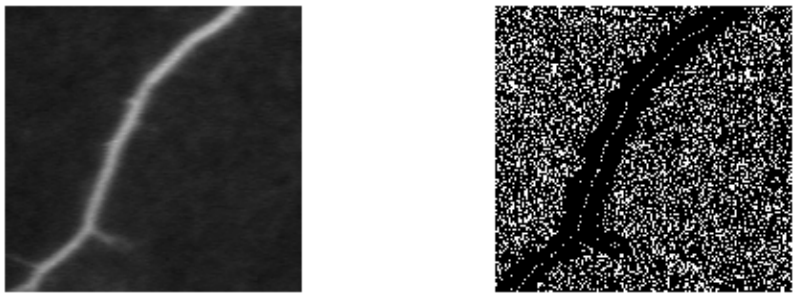

Figure 7.2. Sample extrema map of an FFA image. (a) Sub-part of an FFA image. (b) Extrema map of the sub-part in (a).

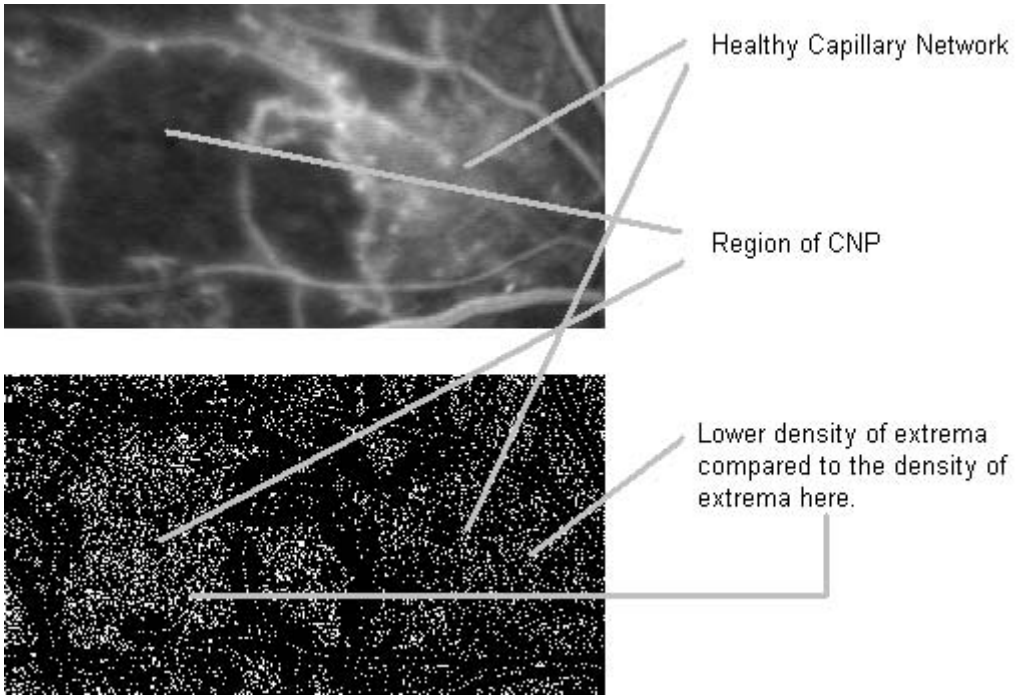

Figure 7.3. The density of extrema in the extrema map of healthy capillary region and a region of CNP.

in the density of extrema in the CNP regions and healthy capillary network is visually noticeable only on carefull observation. Though the difference is visually subtle, it can be exploited quantitatively to formulate CNP segmentation algorithms. Such an approach to segmentation of CNP is presented in the next section. An example where the difference in density of extrema is visually noticeable is shown in Figure 7.5.

7.3. Segmentation of HRA images

The CNP segmentation algorithm we propose is based on the properties of HRA images discussed in Section 7.2. It exploits the fact that density of the extrema in the regions of CNP is higher than the density of extrema in other retinal regions. The segmentation is achieved by extracting regions where the density of extrema is higher than a certain threshold. A block diagram, of the various processes involved, is shown in Figure 7.4. Most HRA images are corrupted by noise. Hence, the segmentation algorithm should typically be preceded with a noise filtering operation as shown in the figure.

The various steps of the algorithm, in the order of operation, are as follows.

i. **Extracting the extrema map**

The first step, after the optional noise filtering operation, is to extract the extrema-map from the FFA image. This is done my extracting all the local minima and maxima in the image. A pixel is defined as an extremum pixel if it is greater than or equal to all of its 8-connected neighbours, or if it is less than or equal to all of its 8-connected neighbours.

ii. **Cardinality filtering**

In the next step, extremum pixels lying in regions of low density of extrema are filtered out. This is done by a procedure called the 'Cardinality Filtering' which is performed as follows. The number of extrema in a certain neighbourhood around an extremum pixel is found. If this number is greater than a threshold value η, than the extremum pixel is retained, else it is removed from the set of extrema. Performing this operation for all the extrema extracted in the first step will retain only those extrema which lie in regions where there is a high density of extrema. These regions correspond to the regions of CNP in the image.

iii. **Dilation**

After cardinality filtering, the resultant extrema map has only those extrema which are in the regions of high density of extrema. A region of CNP can be formed from a region of extrema 'dots' by filling in the 'gaps' between the dots. This is done by performing a binary morphological dilation.

iv. **Median Filtering**

The dilation operation of the previous step moves the boundaries of adjacent regions closer than the actual perceptual boundaries. Moreover, there are few small black 'islands' within the regions formed after dilation. To move the boundaries apart, and fill-up the islands simultaneaously, a median filtering is performed on the result of dilation.

v. **Region growing and boundary extraction**

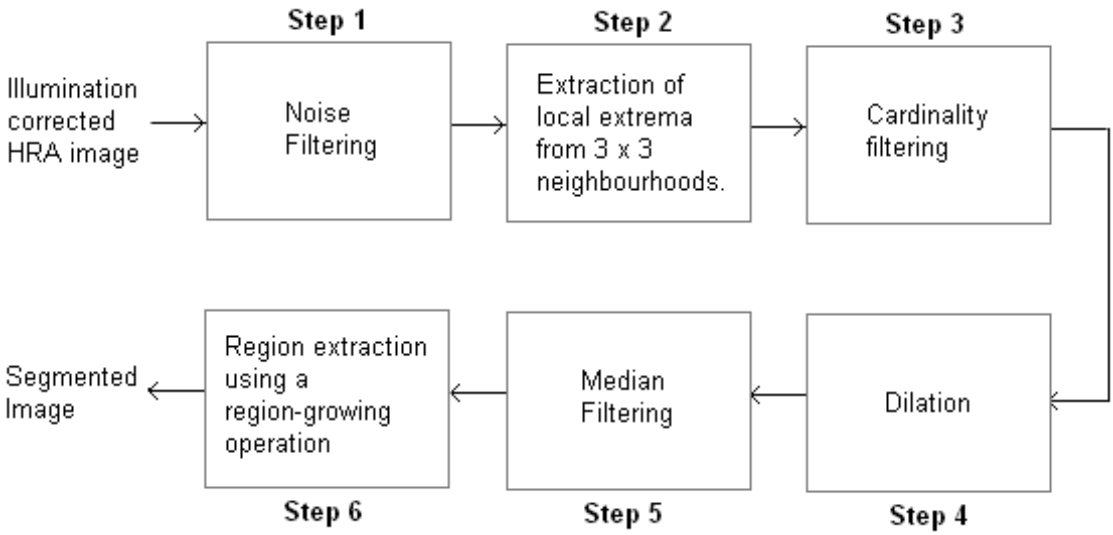

Figure 7.4. Processing steps in the proposed HRA-image segmentation.

The final step extracts the regions of CNP and their boundaries from the result obtained after the median filtering operation. The regions are extracted by a simple region-growing operation following which the boundaries can be extracted using a gradient operation. The area of the CNP regions is obtained from the size of the regions grown during the region-growing step. The percentage of the area of CNP regions can be used as a quantitative measure of the extent of CNP.

To illustrate the working of the various steps, the above algorithm was applied to a sub-part of an FFA image. The image was selected such that the difference in the density of extrema can be noticeable visually. The results obtained after each step are shown in Figures 7.5(a)-(f). The result of extracting the extrema-map is shown in Figure 7.5(b). One can clearly see that the healthy capillary network has a lower density of extrema. The extremum pixels in such a region are filtered out by the cardinality filtering operation as see in Figure 7.5(c). The result of dilation and subsequent median filtering are shown in Figures 7.5(d)-(e). The final result, after extracting the boundaries of the regions formed after median filtering, is shown in Figure 7.5(f).

7.4. Results and discussion

The proposed algorithm was implemented as follows. First, all local extrema were extracted using a 3×3 window. Next, cardinality filtering was performed using a 11×11 window and with a cardinality number of 25. The dilation was performed using a 3×3 rectangular structural element. The median filtering operation, using a 3×3 window, was performed before the final region growing and boundary

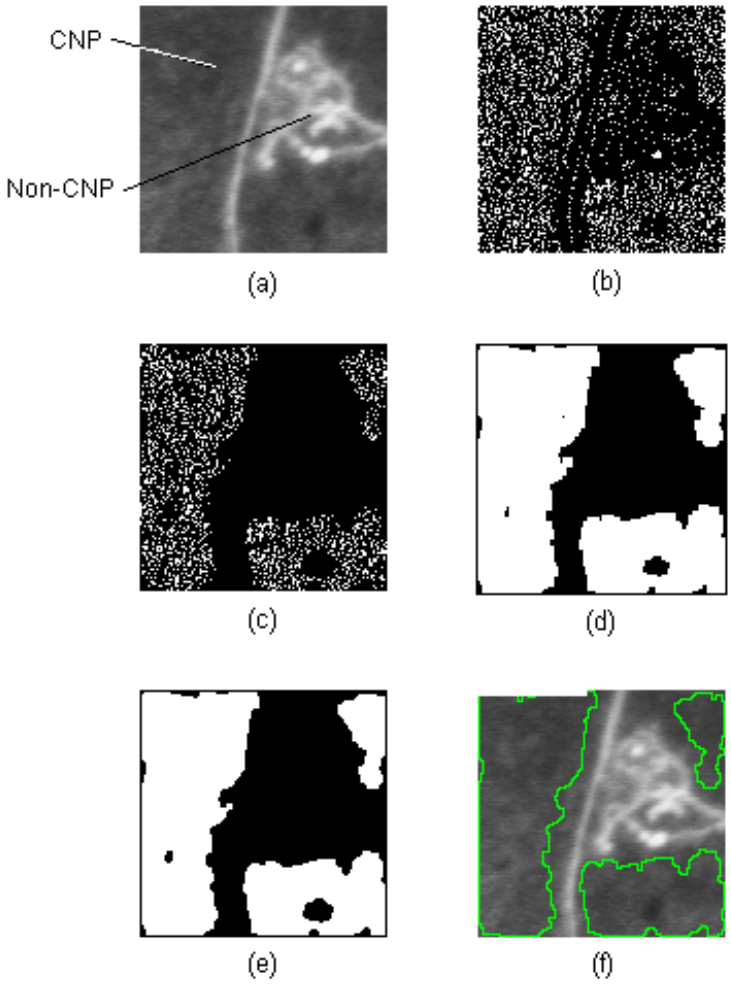

Figure 7.5. Results at different stages of the HRA segmentation algorithm.

extraction operations. The results of this on two HRA FFA images are shown in Figures 7.6 to 7.11. For each FFA test image, a ground truth image, and an image with the result of segmentation are shown in order. The ground truth was marked by a retina expert to indicate the different regions of CNP in an image. To avoid tedious boundary marking, the different regions of CNP were marked by a white dot. Each white dot in these images corresponds to a region of CNP around it. The white lines in the result images correspond to the boundaries of the segmented CNP regions.

As can be observed from the results, the segmentation algorithm detects most of the regions of CNP. However, one can observe that CNP regions of small size are missed. This happens because of the following reason. As mentioned earlier in the chapter, the injected dye continuously effuses out the retinal membranes. This phenomenon is absent in the regions of CNP as the dye does not reach such regions. However, dye from the surrounding regions can cloud small regions of CNP. Consequently, the

density of extrema in such regions will be lower than the density of extrema in larger regions of CNP and hence, are not detected.

The proposed algorithm is based on a hypothesis that the regions of CNP have a higher density of extrema as compared to other regions. However, such a hypothesis need not hold always. One reason is that if the dye effusing over a healthy capillary network is negligible, then such regions will also have a high density of extrema. Another important reason for the failure of this hypothesis is that the HRA images are corrupted with noise and this noise corrupts even the vascular regions, leading to a high density of extrema on the blood vessels. In such extrema maps, it will be hard for even a human oberver to visually distinguish between a vasculature region and other regions. To overcome corruption by noise, one could start by filtering out the noise as shown in Figure 7.4. This noise filtering will also smoothen the minute choroidal capillary texture of regions of CNP. However, even in such cases, the extrema-map of a CNP region and that of a region of healthy capillary network will differ in the similar fashion as claimed in the hypothesis. This happens because the minute texture of the CNP regions is transformed into flat regions which, by our definition of extrema from Section 7.3, form huge chunks of minima, while the texture of a healthy capillary network is transformed into a very gradually varying, 'bumpy' terrain with very sparse minima and extrema. Hence, one can expect that the hypothesis can be used in case of both noisy as well as noise free images.

The algorithm was tested on 62 HRA FFA images. Of these, 12 were provided to us initially for understanding and algorithm development. These images were either noise free or corrupted with a small amount of noise. The algorithm yielded good results on these 12 images. This can be observed in case of two the test images 1 and 2 shown in Figures 7.6 to 7.11. However, the rest 50 were provided to us on a much later date and were corrupted by large amounts of noise. The performance of the algorithm degraded heavily on these images even after Gaussian noise filtering. An example of a noisy image (test image 3) and the corresponding result of segmentation is shown in Figures 7.12 and 7.14. The detected regions of CNP do not match the ground truth as the boundaries of the segmented regions cut across the blood vessels. This happens because of high density of extrema even over the blood vessels.

7.5. Conclusion

Extraction of regions of CNP from FFA images is a function of the disease analysis module of the framework proposed in Chapter 3. In this chapter, a novel technique for such an extraction from HRA FFA images was proposed. Though this technique yields good results on noise-free HRA FFA images, the performance degrades in the presence of noise. In order to use the technique on a wide variety of images, one will have to develop an efficient noise removal technique which does not swamp the fine capillary texture while removing the noise. Design of such a technique is not a trivial task. Alternatively, the approach to the CNP segmentation problem can be formulated using a stochastic model for CNP regions. Both of these approaches were considered to be out of the scope of this thesis.

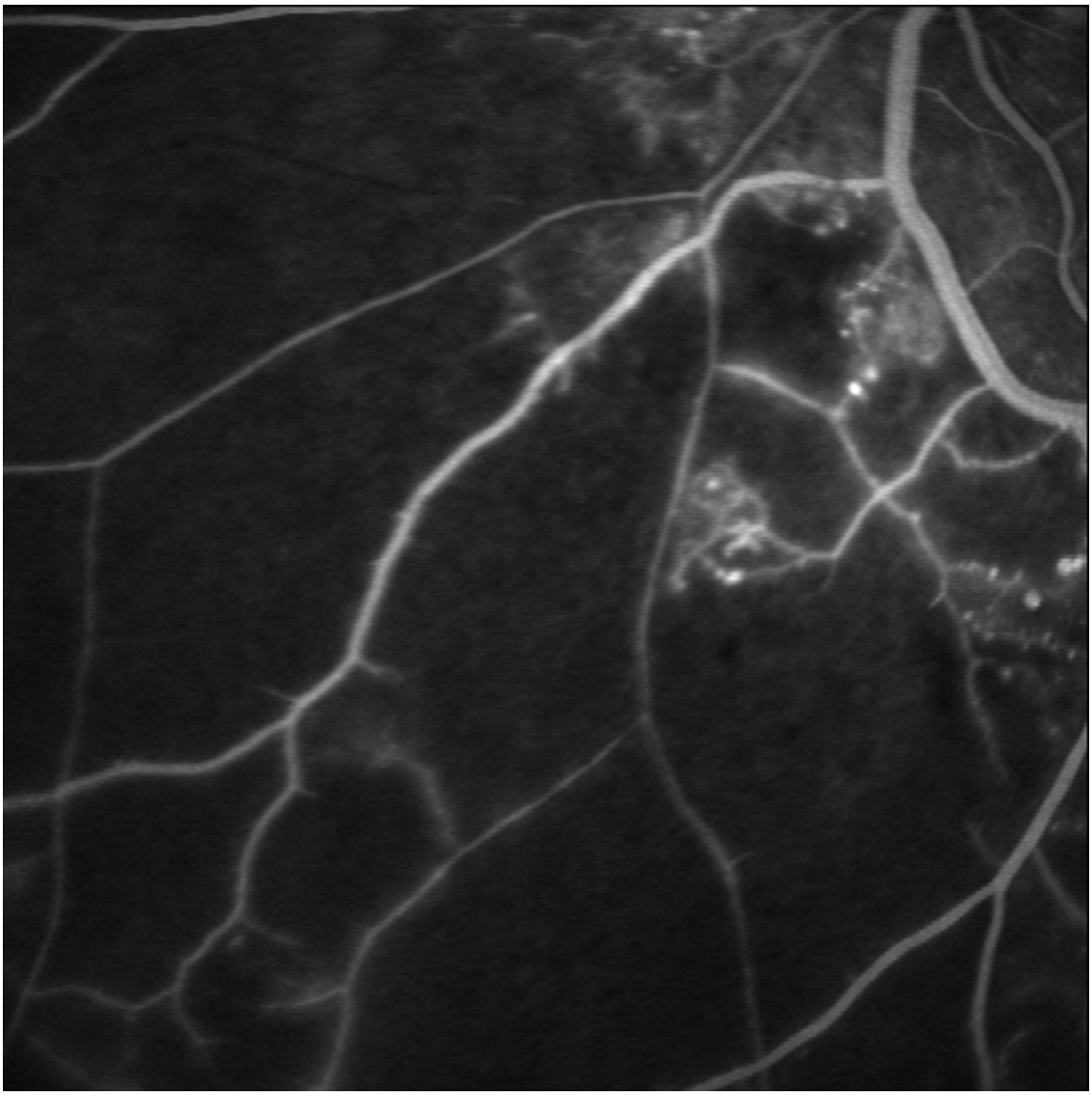

Figure 7.6. FFA test image 1.

The proposed technique exploits the fact that the choroidal capillary network is also seen through regions of CNP in an HRA image. Hence, it cannot be used in case of the Zeiss images where the optical camera cannot capture the choroidal capillary network. However, there is scope to apply this technique for segmentation in other domains (non FFA images) where images have fine wooly textural patterns similar to the texture of capillary network in an HRA FFA image.

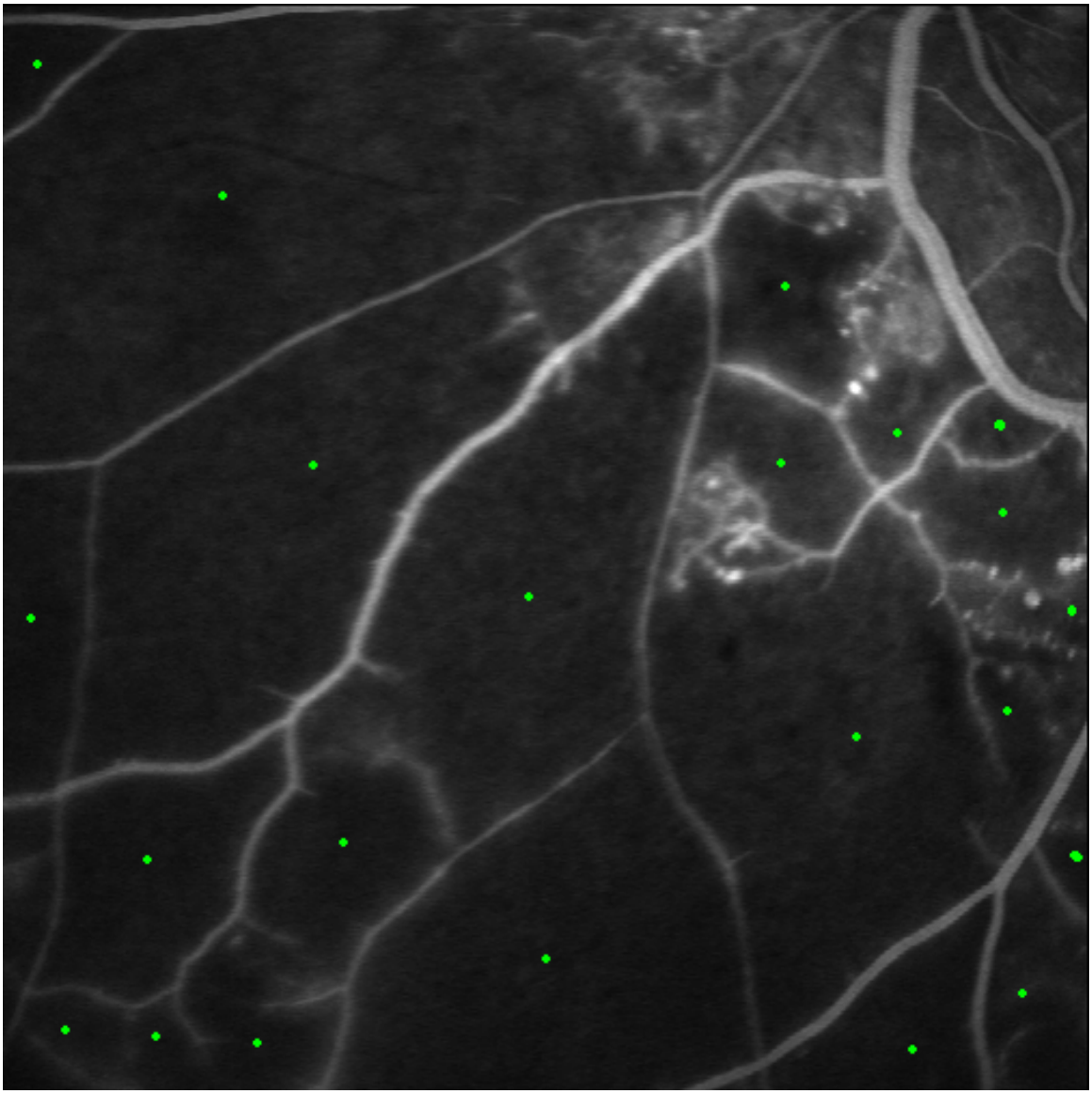

Figure 7.7. Ground truth marking of the test image 1.

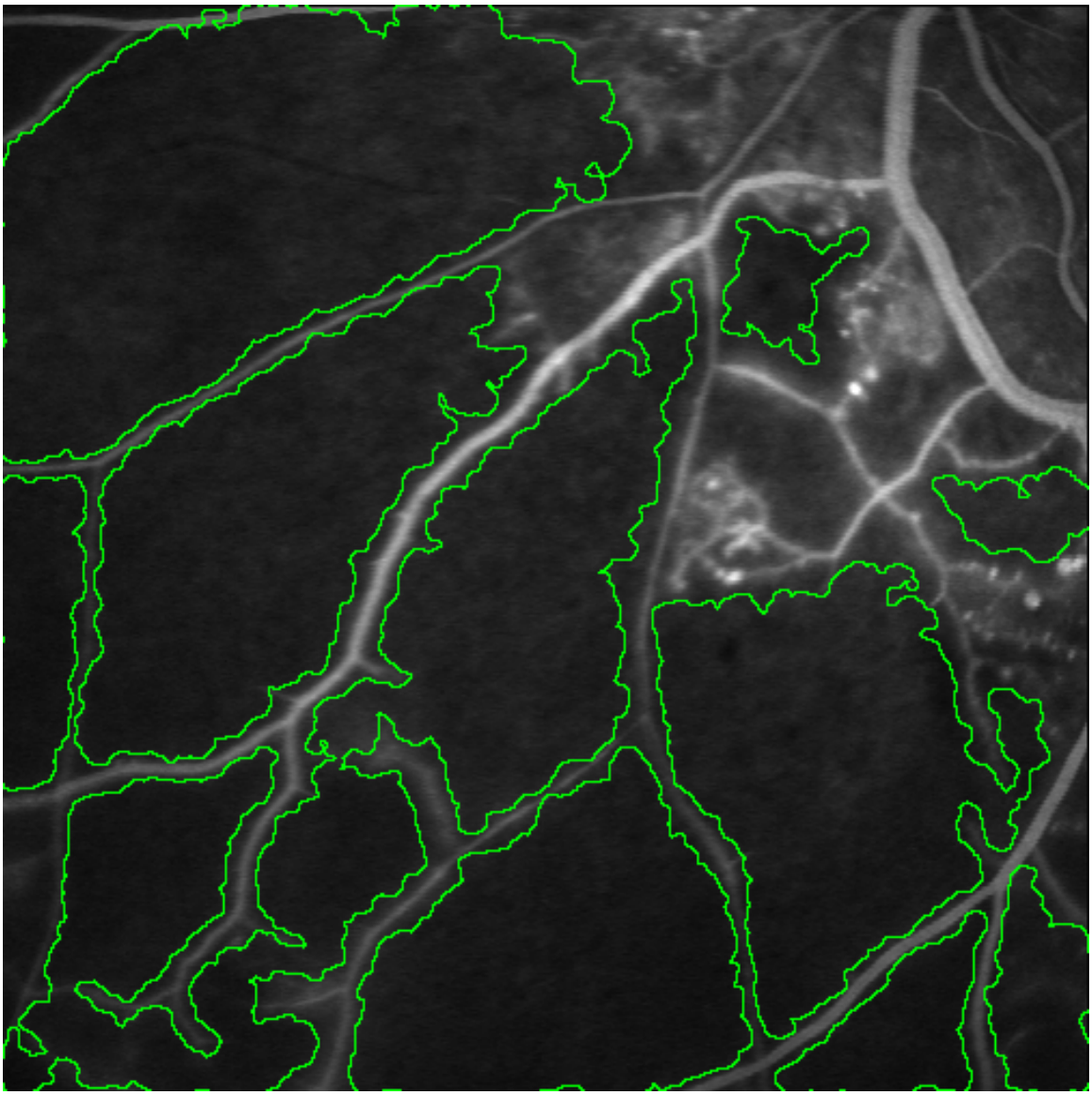

Figure 7.8. Result of segmentation of the test image 1.

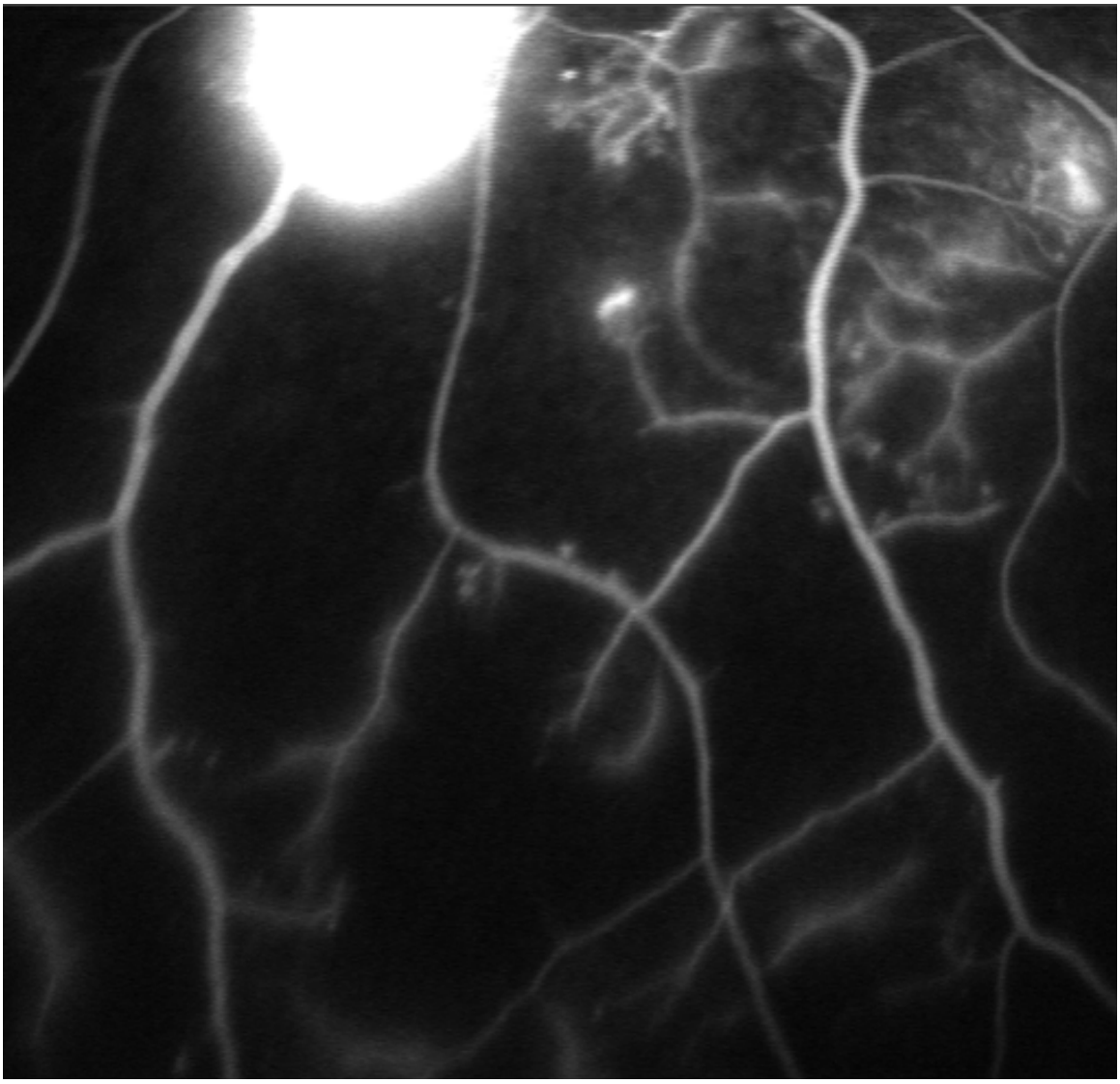

Figure 7.9. FFA test image 2.

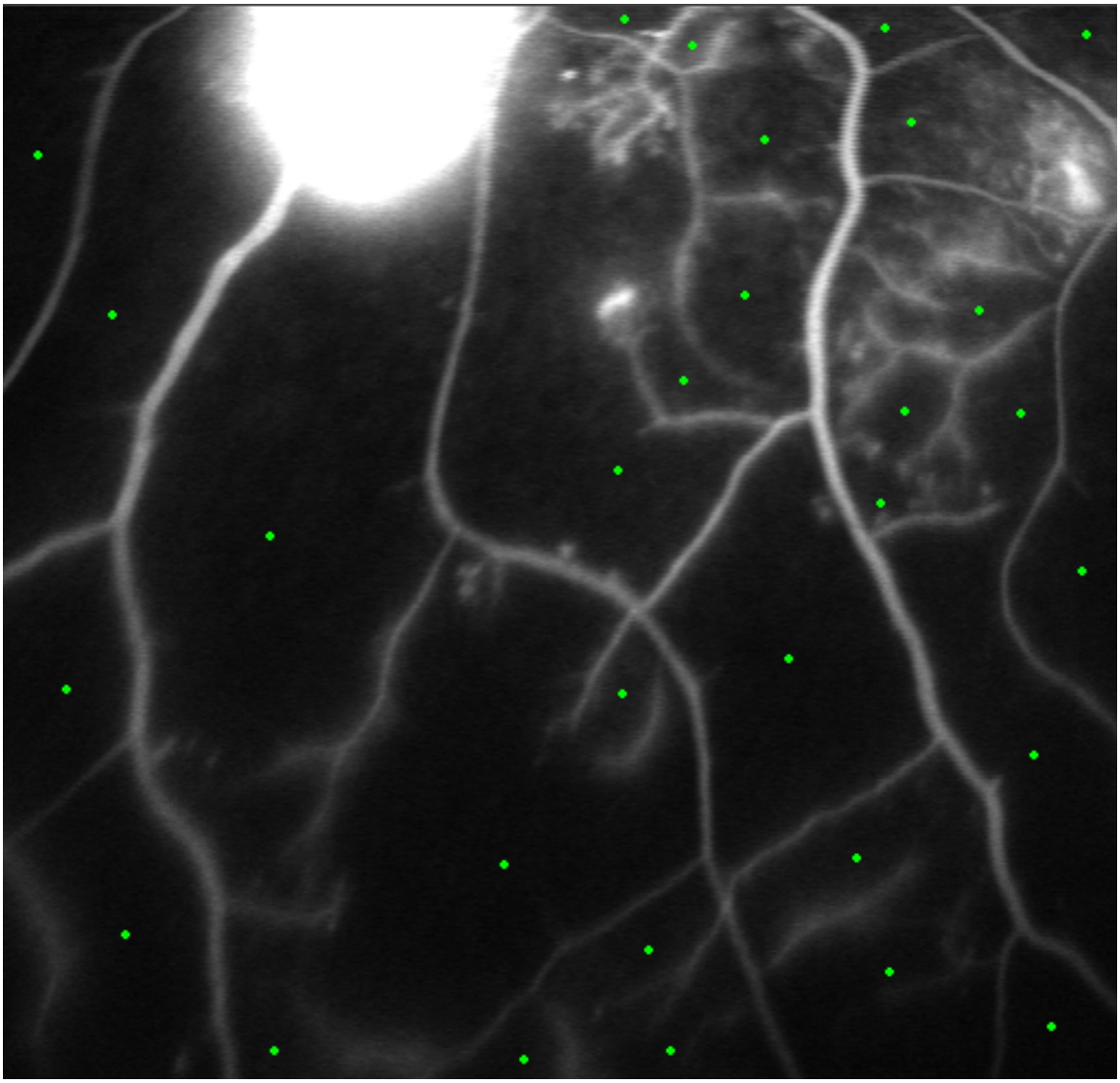

Figure 7.10. Ground truth marking of the test image 2.

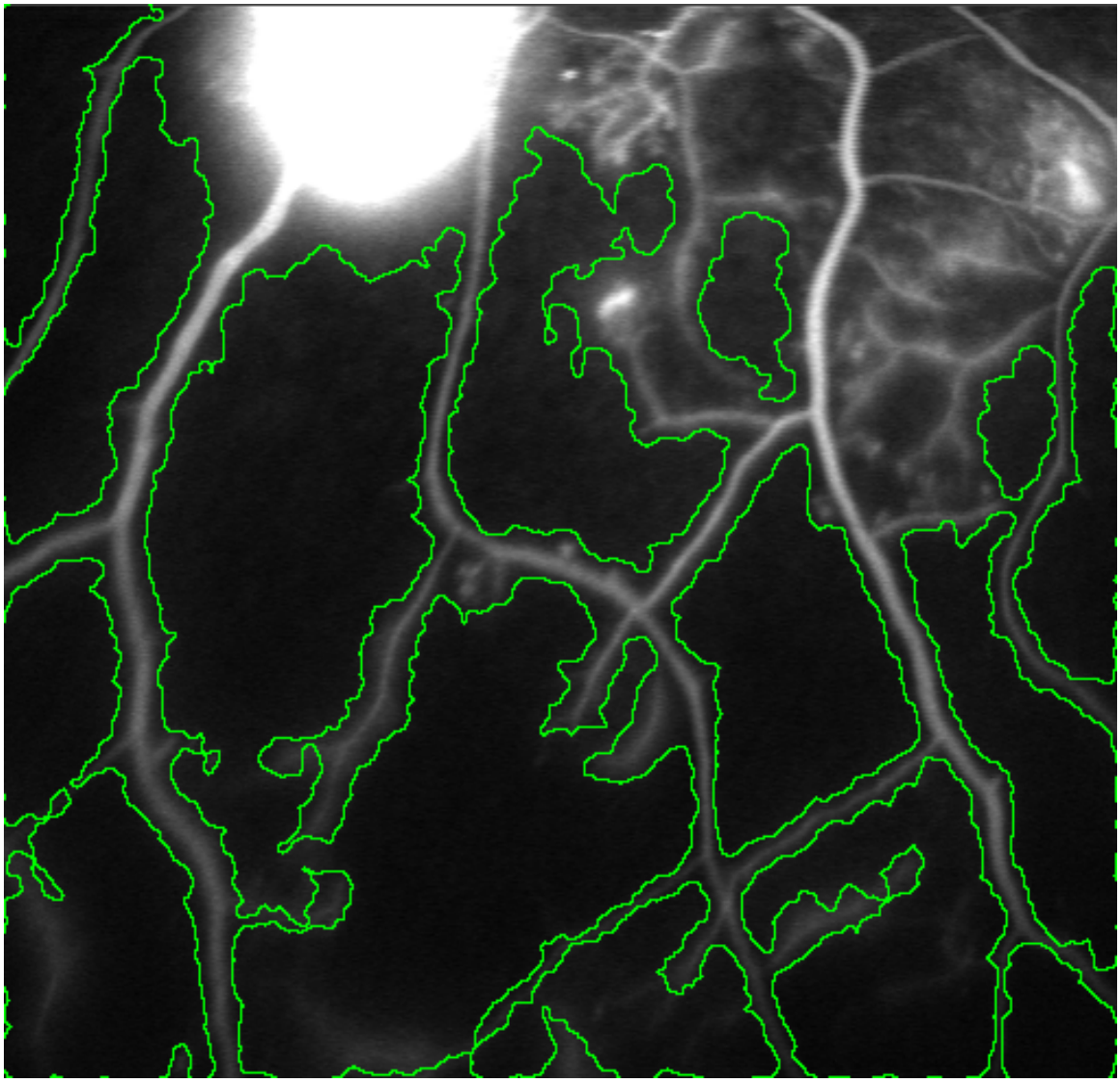

Figure 7.11. Result of segmentation of the test image 2.

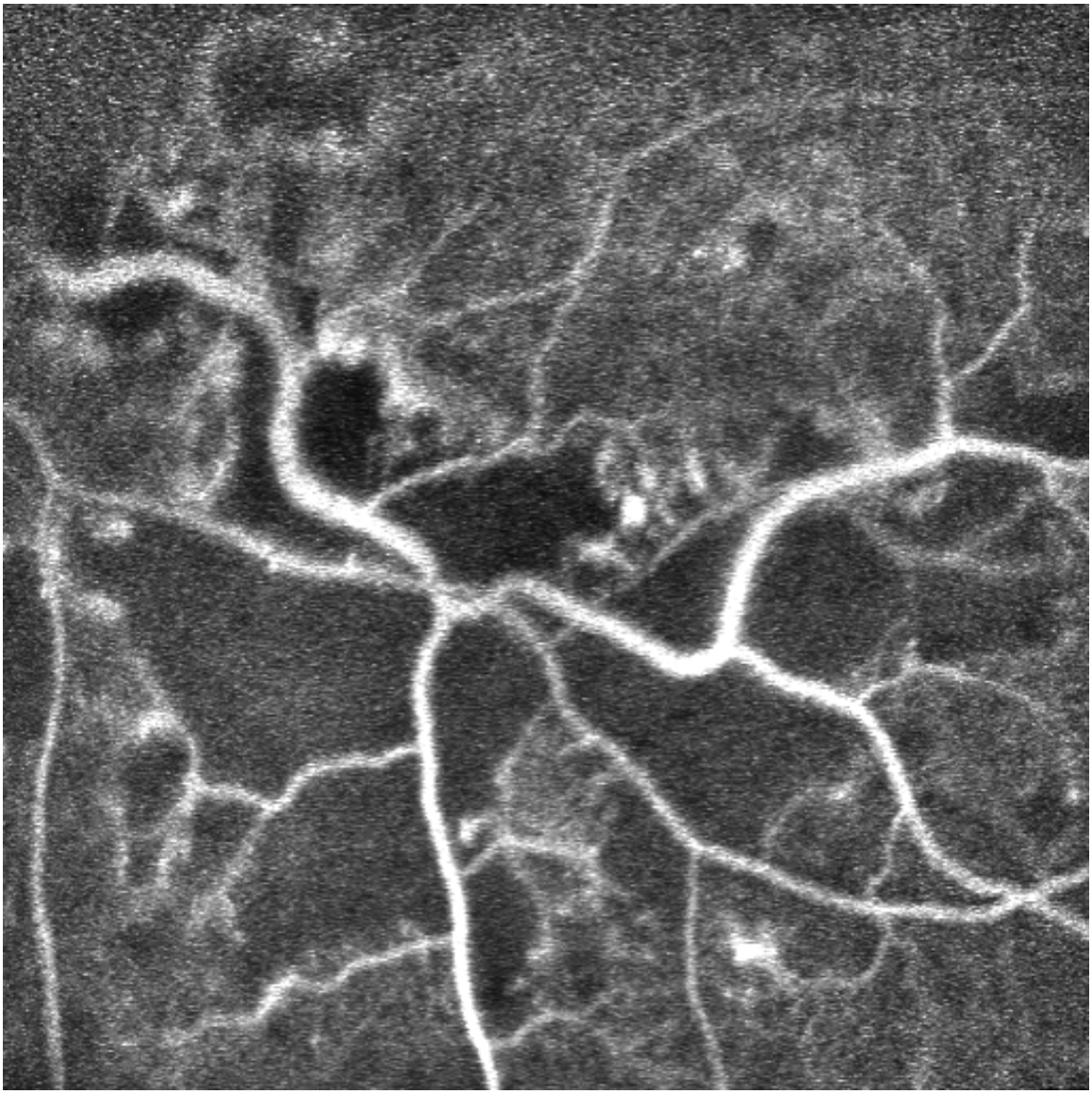

Figure 7.12. FFA image 3.

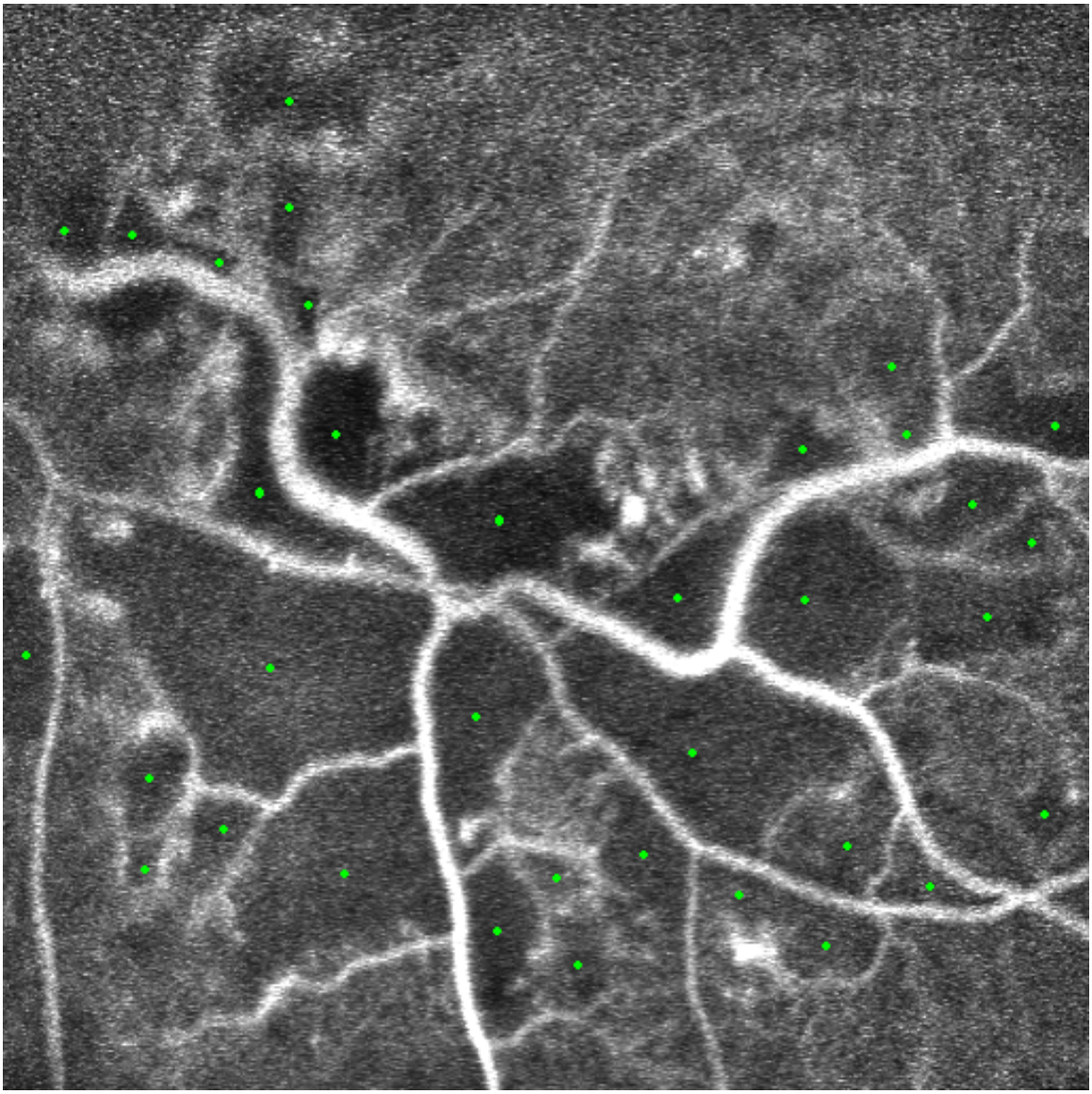

Figure 7.13. Ground truth marking of the test image 3.

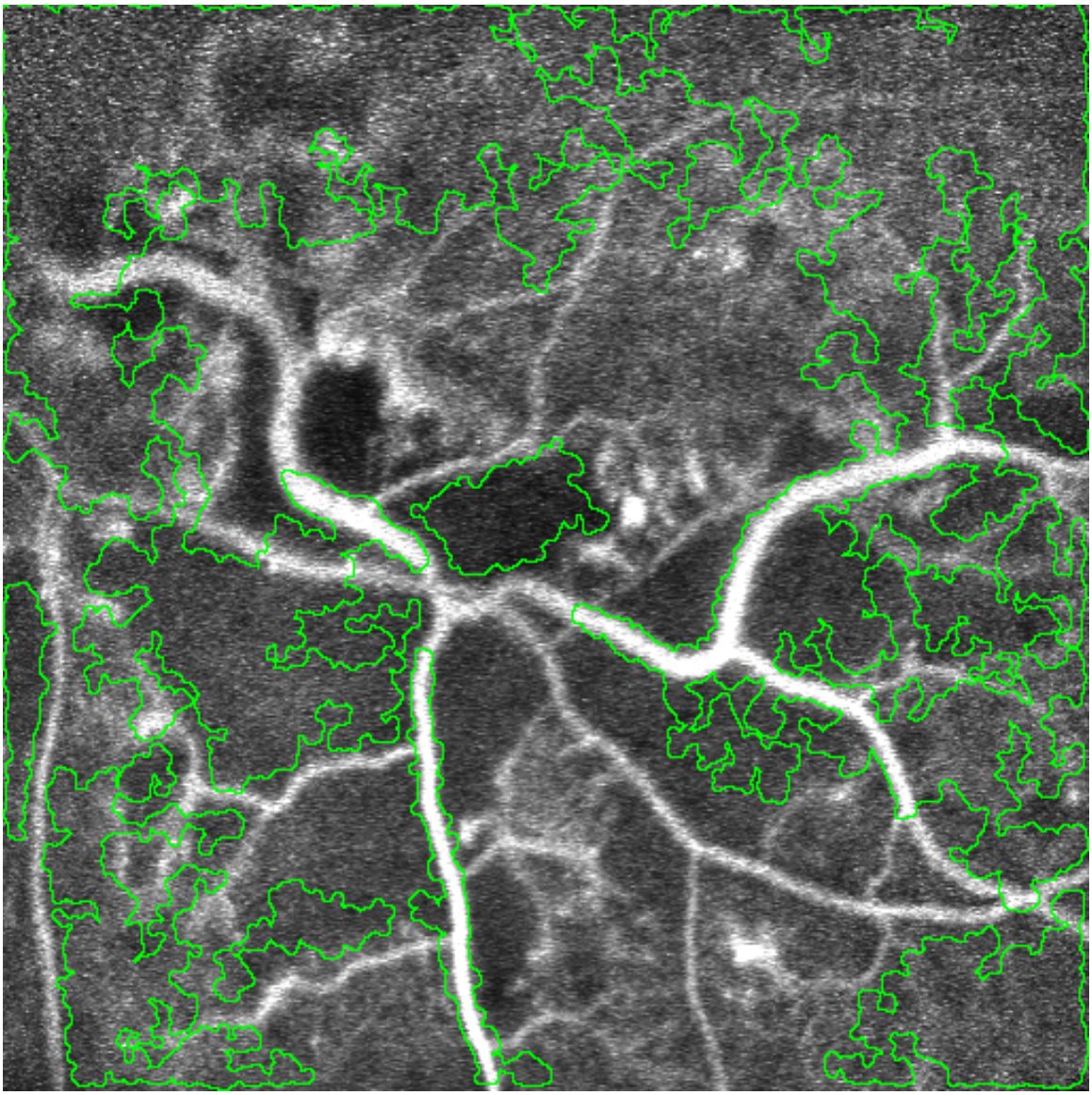

Figure 7.14. Result of segmentation of the test image 3.

Chapter 8. CNP Analyser - A tool for extraction of regions of CNP

8.1. Introduction

A framework for retinal angiogram image (or FFA image) analysis was proposed in Chapter 3. As mentioned in chapter 1, the most common aim of FFA image analysis is to detect diabetic retinopathy (DR). Though DR causes two different kinds of defects namely, Microaneurysms and CNPs, detection of CNP from FFA images forms a more important problem. This is because of two reasons: (i) Regions of CNP can be distinguished from other regions only in FFA images. (ii) CNP occurs in the later stages of DR and needs immediate attention. Hence, to provide a diagnostic aid to the retina experts a tool called 'CNP Analyser' was built which aids in the detection of CNP and showcases the framework proposed in Chapter 3. In this chapter, we present a description of the design of this tool.

8.2. CNP Analyser

As mentioned in Chapter 2, FFA images suffer from many problems. A disease extraction tool should solve these problems before detecting the diseased regions. A modular framework, developed with such a principle, was proposed in Chapter 3. The 'CNP Analyser' tool was built using this framework. The various operations which have to be incorporated into a CNP extraction tool are as follows.

1. **Illumination Correction**

   Most FFA images suffer from poor/non-uniform illumination. This problem has to be rectified by a suitable illumination correction step in the pre-processing module.

2. **Noise Filtering**

   Noise filtering is also a function of the pre-processing module. Noise changes the textural appearance of the retinal regions and can lead to wrong diagnosis. Hence, it has to be removed before a CNP extraction step.

3. **CNP Extraction**

   The main task of a CNP detection tool is the CNP extraction operation. CNP extraction should be performed after the illumination correction and noise fitering steps.

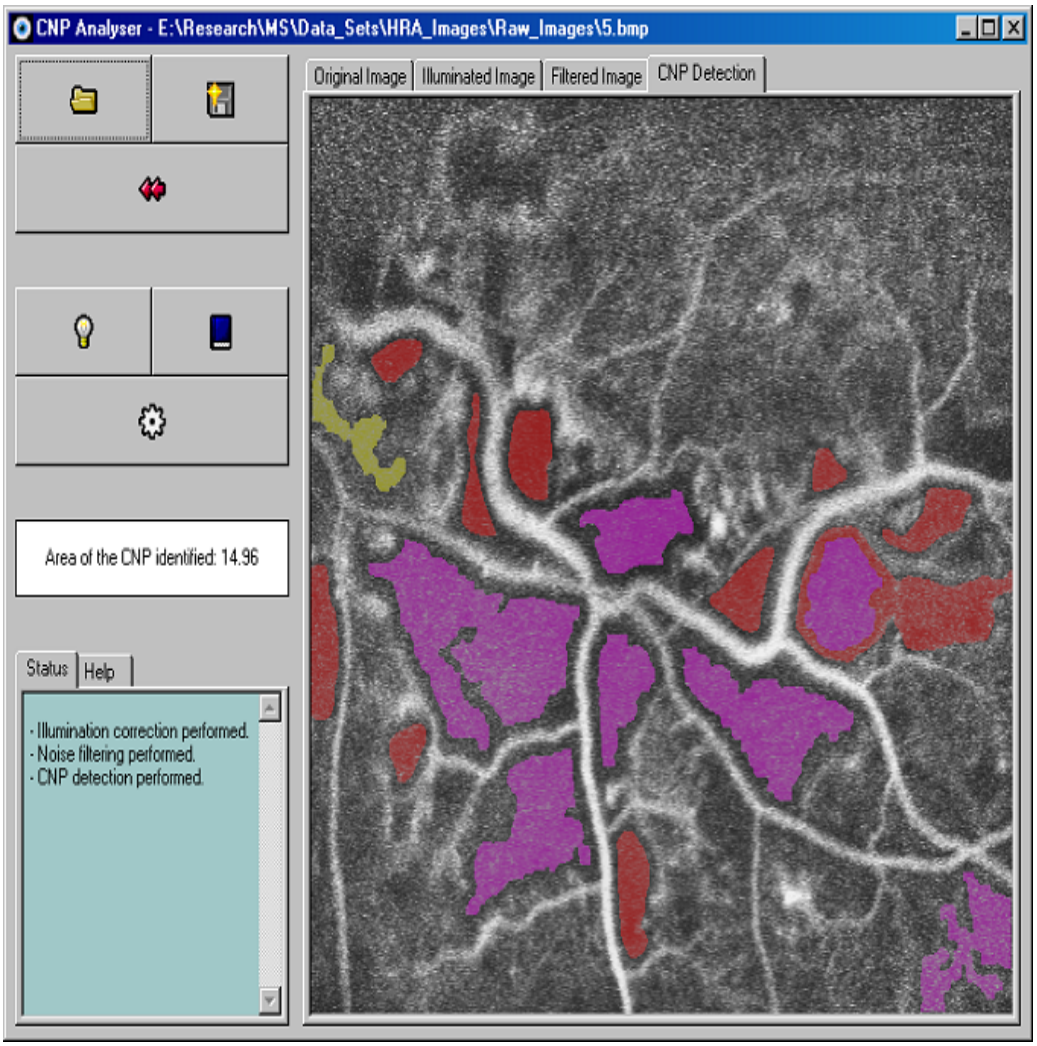

Figure 8.1. A screen-shot of the 'CNP Analyser' tool.

4. **Interactive Add-Remove facility**

   CNP extraction is typically performed by using an image analysis step which does not make use of any higher level knowledge about the regions of CNP. Hence, few regions of CNP may not be picked while other non-CNP regions may be classified as regions of CNP. As the tool is developed with aim that it has to aid in the diagnosis of CNP, a facility to add/remove misclassifications should be provided.

5. **Quantification**

   The extent of the damage due to CNP should be quantified using some measure and displayed on the main window after the CNP detection operation. This measure should relect the changes made

with the add/remove facility.

The screen-shot of the CNP Analyser is shown in Figure 8.1. It was developed in the C++ programming language using the wxWidgets 2.4.2 GUI library [34]. All the above features have been incorporated. The illumination correction step is performed using the algorithm proposed in Chapter 4. The noise filtering step is performed using a 15×15 Gaussian mask with a standard deviation of 5. CNP extraction is performed using the segmentation algorithm proposed in Chapter 7. The extraction step marks the candidate regions of CNP with a magenta tint. A retina expert can add and remove regions by clicking. Regions removed by clicking get marked by a yellow tint, while the regions added by clicking get marked by a red tint. The extent of CNP is quantified using the percentage of the area of the regions of CNP and is displayed on a text label on the main window of the tool.

8.3. Performance

The tool was tested using 50 noisy images. A quantitative study of the results was not performed as this tool was partly interactive. As expected, it falsely detects few regions and misses out detection of few other regions of CNP. Though the number of clicks to arrive at the final result was high, retina experts who tested the tool found that the interactive add and remove facilities were useful in removing the shortcomings of the CNP segmentation algorithm.

The operations incorporated into the tool are implemented in a modular fashion. Hence, one can plug in different algorithms for illumination correction, noise filtering, and CNP extraction, depending on their choice.

Chapter 9. Summary and Future Work

Summary

In this thesis, a modular framework for a generic retinal angiogram (FFA) image analysis system was proposed (Chapter 3). The frame work consists of four modules, namely 1) Pre-processing module, 2) Retinal structure analysis module, 3) Disease analysis module and 4) Classification module. Specific instances of these modules as illumination correction (Chapter 4), blood vessel Detection (Chapter 5), microaneurysm detection (Chapter 6) and CNP segmentation from HRA images (Chapter 7), were presented. A tool to detect regions of CNP was developed to showcase the proposed framework.

Most FFA images suffer from poor/non-uniform illumination. Illumination correction is a function of the pre-processing module. In this thesis, a solution to the problem of non-uniform illumination was proposed by modelling the degradation function as a multiplicative effect. It was shown that this technique removes the effect of non-uniform illumination and adjusts the image to the right levels of brightness and contrast, hence not requiring any high level information about the retinal structure.

Blood vessels form the most important structure features of a retina. Detection of blood vessels is a function of the struture analysis module. In this thesis, the blood vessel detection algorithm was formulated by modelling them as topographical ridges. Due to its ability to detect a wide range of ridge profiles, a curvature based ridge detection algorithm was choosen to detect the blood vessels. An efficient and elegant technique, called the surface tangent derivative (STD), was proposed to estimate the curvature of the image surface. Single scale as well as multiscale ridge detection algorithms were formulated using this novel estimate.

Microaneurysms are baloon shaped sprouts of new capillaries in the retina. They occur as tiny disk-like structures in an FFA image. Detection of MAs is a function of the disease analysis module. In this thesis, the MA detection algorithm was formulated by modelling MAs as hill-like topographical features of the image surface. MAs were located at points were the curvature of the image surface is a maximum in *all* directions. The STD value was again used as an estimate of the surface curvature.

Regions of CNP are areas in the retina where the capillary network has stopped supplying blood. They occur as dark lesions in an FFA image. In this thesis, a novel CNP segmentation algorithm using an interesting property of the HRA images was developed. This technique was found to perform well on noise free HRA images. However, it suffers from high sensitivity to presence of noise in the images.

Future Work

Handling Montages

In this thesis, the framework and the analysis techniques were proposed only for a single FFA image. However, as mentioned in Section 2.2, the entire retina cannot be captured in one single image. Different parts of the retina are captured in different images. These different images are then 'Montaged' or 'stitched' together to let a human expert see the big picture. Likewise, the framework and analysis techniques should be extended to handle these montages.

One possible way to handle multiple images is as follows. The individual images have to be analysed using the proposed single-image framework. The results obtained should then collated efficiently to arrive at one single measure for the extent of a disease in the entire retina. For this, efficient techniques have to be formulated to collate results obtained from analysis of individual images.

Classification of Candidate Regions

As we have seen in the previous chapters, image analysis techniques can only detect candidate regions affected by a particular disease. These candidate regions will have to be classified into true positives and false positives. Hence, efficient classification techniques which use higher level charaterics of the disease regions should be formulated for this purpose.

Incorporating Time-Stamp Information

It was mentioned earlier that the injected dye continuously effuses out of the vascular membranes. This effusing dye degrades the quality of the image with increase in time from when the dye was injected into the patient's body. Hence, it will be usefull to incorpotate the time-stamp information of the image files into the classification schemes as it will help in assigning a measure of truth to the detected disease regions.

Disease Tracking

It is important to track the progress of a disease, under treatment or otherwise, in order to devise efficient treatment procedures. Tracking a disease involves detecting changes in the images obtained over a number of visits. The images have to be first aligned, along the retinal structure, before detecting changes. Hence, efficient change detection and image registration schemes should be developed in order to facilitate disease tracking.

Publications

To date, there have been three accepted/under review publications using the work presented in this thesis. Their details are listed below.

1. Taraprasad Das, Jayanthi Sivaswamy, B. R. Siva Chandra, Alka Rani, Vindhya Vunnum. 'Computer aided quantification of capillary non-perfusion and drusen'. National Retina Congress, LV Prasad Eye Insititute, Hyderabad, India 26th - 28th August 2005.

2. B. R. Siva Chandra and Jayanthi Sivaswamy. 'Illumination correction of Colour Retinal Images'. Proceedings of the SPIE Symposium of Medical Imaging, San Diego, 2006. (To appear)

3. B. R. Siva Chandra and Jayanthi Sivaswamy. ‘An Analysis of Curvature Based Ridge and Valley Detection’. IEEE Intl. Conf. of Acoustics, Speech and Signal Procc. 2006. (Under review)

Appendix A. Image Surface

A 2D digital image is a function of two independent and discrete variables. It can be visualised as a surface in 3D space. In this appendix, we shall formalise these notions and present definitions for a '2D digital image', an 'image pixel' and an 'image surface'. The notations and conventions presented here are followed throughout this thesis.

The discrete grid over which a 2D digital image is defined is called the base-plane (see Figure A.1) and is defined by the cross product

$$\Gamma = \{0, 1, 2, \ldots, N-1\} \times \{0, 1, 2, \ldots, M-1\} \tag{A.1}$$

where M and N are the height and width of the image respectively. An ordered pair $(n, m) \in \Gamma$ is called an image pixel. An image is defined as a funtion $I : \Gamma \to \Re$. The *intensity* at a pixel (n, m) is given by $z = I(n, m)$. The image surface is defined as the set

$$\varsigma = \left\{ (n, m, z) \;\middle|\; (n, m) \in \Gamma,\ z = I(n, m) \right\} \tag{A.2}$$

A triplet $(n, m, z) \in \varsigma$ is called a point on the surface ς. The intuitive notion of a base-plane and an image surface is formed by visualising ς as a surface hanging over the plane Γ.

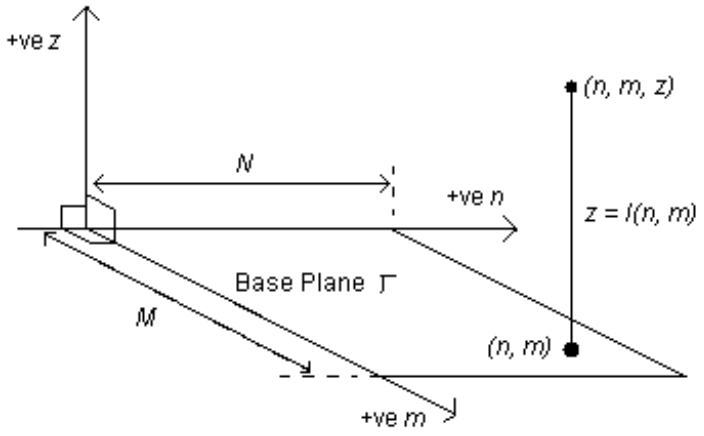

Figure A.1. Geometry of the image function

Appendix B. Locating the Circular Aperture in Zeiss Images

Images obtained using the Zeiss system have a circular aperture within which the retinal regions are captured. To process or analyse such images, the location of the center of this aperture and its radius have to be extracted as a pre-processing step so that the analysis procedures can be confined to this aperture. In this appendix, we will present a procedure to extract the center and radius of such an aperture. A typical example of an image captured using Zeiss systems is shown in figure B.1(a).

A property of Zeiss images which is used in the aperture location technique is as follows; The circular parts of interest are bounded by dark regions. These regions can be seen in both figure B.1. The property of these dark regions is that they are of uniform intensity. For example, if the intensity value of the top-left-corner-pixel is 10, then the entire dark region, on both left and the right sides of the image, is guaranteed to be of intensity 10.

Using the above property, we can reasonably expect that by thresholding the entire image by a threshold value of $T = I_0 + 1$ (where I_0 is the intensity value of the top-left-corner-pixel) we obtain an image with the circular part of the image extracted as a white disk. However, a closer observation of these images reveals that the transition from the dark boundaries to the disk of interest is not abrupt but is a steep gradient. We have found that the disk obtained by thresholding is closer to the perceptual disk of interest if we use a threshold value of $T = I_0 + 3$. In the following discussion, T should be understood to have been defined in this way.

The result of the threshold operation should ideally be a circular disk. But most often, it has been found that few white specks show up around the boundary of this expected circular disk. These can be attributed to some kind of noise creeping up during the imaging process and can be removed by a median-filtering operation. In the results we have presented here, we have performed a median-filtering using a 3×3 mask.

Thresholding followed by median filtering extracts a circular disk from a raw Ziess image. An example of such extraction is shown in figure B.2. The center and radius of the circular aperture are the same as the center and radius of this circular disk. Hence, the next task is to extract center and radius information from the ‘disk-image’. The next section discusses this procedure.

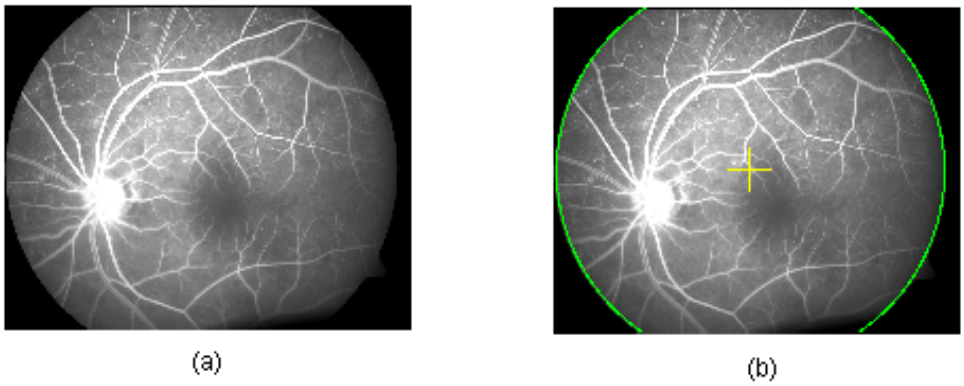

Figure B.1. (a) A sample Zeiss Images. (b) The result of locating the camera aperture.

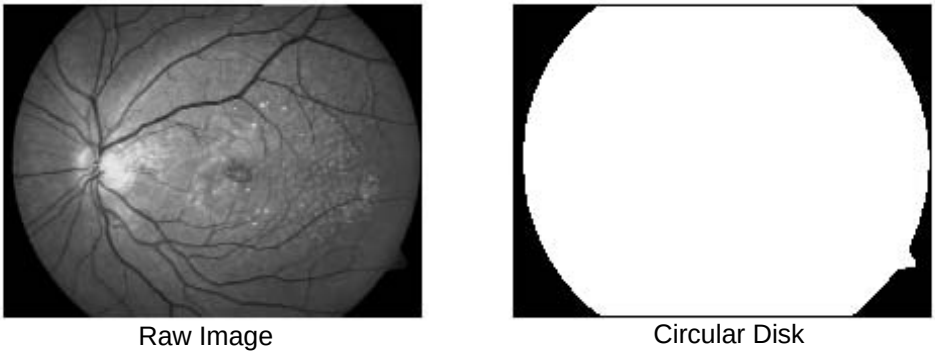

Figure B.2. Example of extraction of the circular disk from a raw Ziess image.

B.1. Locating the center and radius of the circular disk

A point to note before attempting to find the center and radius of the circular disk is that the center of the disk is not the center of the image and is considerably off the center of the image. This happens because of the fact that the center of the aperture is itself off the center of the image. Moreover, parts of the aperture can be clipped off from either the top or bottom or left or right side of the image or from some or all of these sides. This is seen in the disk-image being clipped.

A typical disk-image and the neccesary geometry is shown in figure B.3. Let us traverse along a horizontal line, h pixels from the top, from the left of the image to the right. Then, while traversing, we will reach the disk at a certain distance. Let us call this distance a and the coordinates of the point where this happens as $A(x_1, y_1)$. Similarly, if we traverse along this horizontal line from the right of the image to the left, we will reach the disk again after a certain distance at $B(x_2, y_2)$. Let us call this distance c. If W is the width of the image, then let us define another quantity $b = W - c$. Then, by the symmetry of

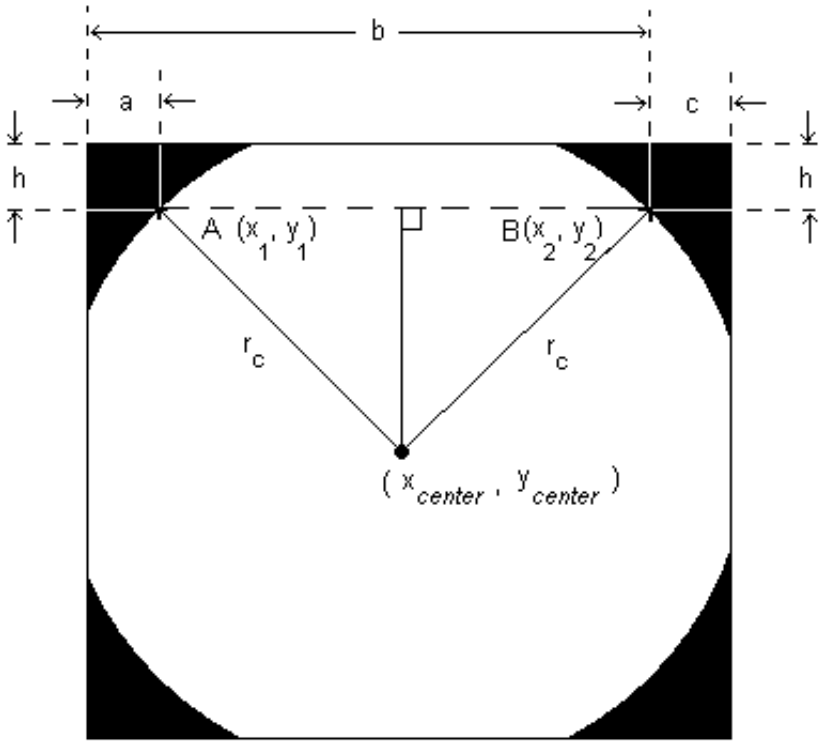

Figure B.3. Geometry for extraction of the center and radius of the circular disk.

the points *A* and *B* about the center of the circle, we can conclude that the x-coordinate of the center of the disk is given by:

$$x_{center} = \frac{a+b}{2} \tag{B.1.1}$$

The y-coordinate of the center of the disk y_{center} is found similarly by traversing along vertical line at a certain distance from the left of the image. Once the coordinates of the center of the disk (x_{center}, y_{center}) are known, we can find the radius of the disk as:

$$r_c = \sqrt{(x_1 - x_{center})^2 + (y_1 - y_{center})^2} \tag{B.1.2}$$

This r_c and the point (x_{center}, y_{center}) are the radius and center of the circular disk respectively and hence, are also the radius and center of the aperture in the Zeiss image resptectively.

The result of locating the circular aperture using the approach presented above is the shown in figure

B.1(b). The aperture and its center are marked in this image.

B.2. Notes

There are a few points that should be noted with respect to the above procedure. Most optical imaging systems add a notch artifact to the circular aperture. This artifact can also be seen in figure B.2. It is added to help a viewer decide the right-side up when using a printed copy. In Zeiss images it is added to the bottom right part of the aperture. Due to this, we could successfully traverse a horizontal line which was a little distance away from the top of the image, and a vertical line which was a distance away from the left edge of the image, to locate the center of the circular disk . However, imaging systems manufactured by other companies might add the notch at a different place. In such cases we should select the right lines, which avoid this notch, to traverse along, and locate the center if the circular disk.

In rare instances, the boundary of the circular aperture might not be clearly defined because of severe illumination problem within it. In such instances, the disk extracted from the image will not align exactly with the aperture. Hence, the radius and center calculated from the image will be offset from the true radius and center. But this occurance is very rare and can be ignored.

Appendix C. Generalised Sobel Masks

The standard Sobel masks (see [10]) of size 3×3 are as shown below (Figure C.1).

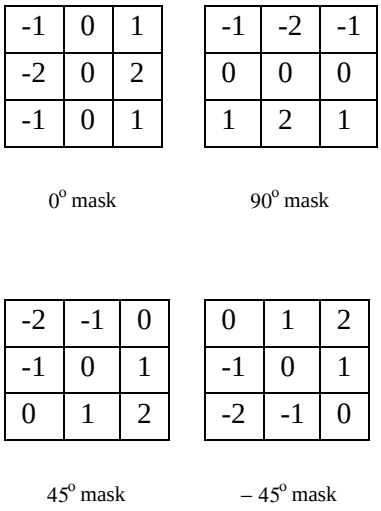

Figure C.1. Standard Sobel masks.

In this appendix we present a generalisation of the above masks to generate Sobel masks of size $n \times n$ where n can be any odd, positive integer. As with the standard Sobel masks, we shall define the generalised masks for four different orientations: $0^\circ, 90^\circ, 45^\circ$ and, -45°.

The notation used in this thesis to refer to a Sobel mask and its elements is as follows. A mask with orientation α and size $n \times n$ is denoted as:

$$\underset{\alpha}{\overset{n}{M}}, \ \alpha \in \Omega = \left\{ 0^\circ, 90^\circ, 45^\circ, \ -45^\circ \right\} \tag{C.1}$$

A mask element is referred by $\underset{\alpha}{\overset{n}{M}}(x, y)$ where x and y are it's indices in the range $-\frac{n-1}{2}$ to $\frac{n-1}{2}$ (n is an odd, positive integer). The reference coordinate system for indexing the mask elements is as shown below (Figure C.2). The sign of the orientation angles is decided using the right-handed system as shown.

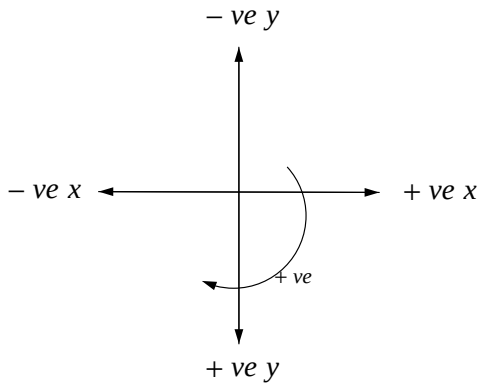

Figure C.2. Reference coordinate system for masks.

The generalisation for generating masks of larger sizes is based on the following points.

i. When an image is convolved with a standard Sobel mask, intensity variations along the orientation of the mask are enhanced. Similarly, the generalised masks should also have directional preference for intensity variations along the orientation of the masks.

ii. There exists a 'line' in the standard Sobel masks, entries along which are zero. Similarly, the central column of the 0° mask, the central row of the 90° mask, the -45° diagonal of the 45° mask, and the 45° diagonal of the -45° mask should be filled with zeroes.

iii. The standard Sobel masks are divided into two halves by the zero entry line. The values in the negative half are negative reflections of the values in the positive half, about the zero entry line. Accordingly, the generalised Sobel masks should also have similar divisions into positive and negative halves.

Using the points (i) and (iii) as guidelines, values in the positive half of a mask are filled as follows (the side of the positive half is determined by the orientation of the mask):

$$\underset{\alpha}{\overset{n}{M}}(x,y) = \frac{1}{1+\left(\dfrac{\theta-\alpha}{\theta_0}\right)^k} \tag{C.2}$$

where θ is the angle made by the mask element (x,y) with the x-axis of the reference coordinate system, θ_0 is a constant less than 90°, and k is a positive even integer. The corresponding zero entry line should be filled with zeroes to satisfy the point (ii). The values in the negative half are then filled using negative reflections of the values in the positive half, as prescribed by point (iii).

In our implementation for this thesis, we have used a value of 60° for θ_0 and value of 6 for *k*. The angular profile of the values in a 0° mask generated using using these values is shown in Figure C.3. One should take care of the fact that an angle of the form $(180^{\circ} + \beta)$ is equivalent to $(\beta - 180^{\circ})$, for some β, while implementing equation C.2.

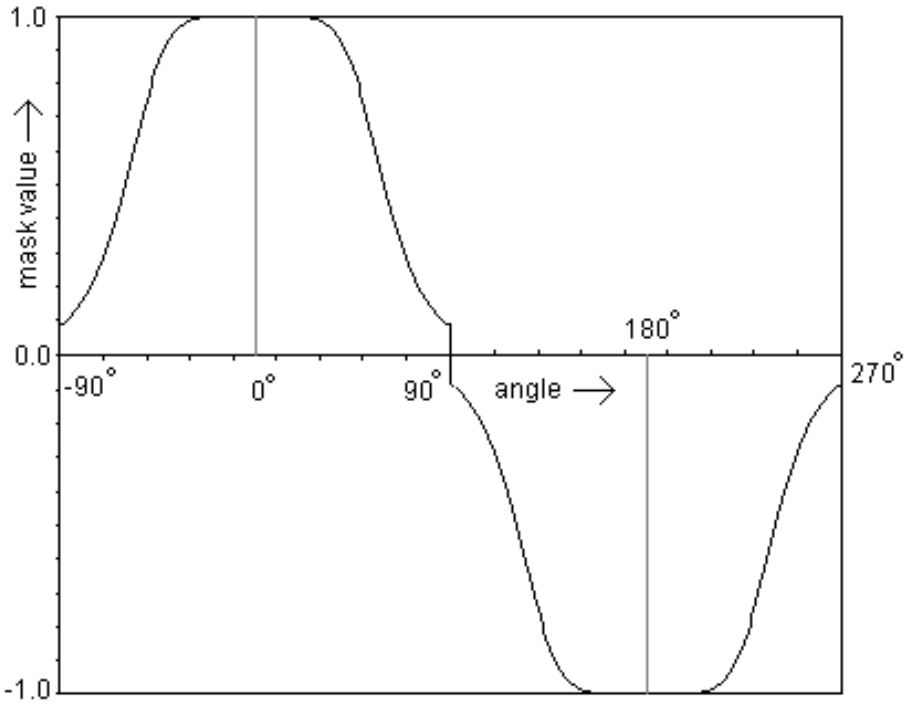

Figure C.3. Angular profile of a 0° mask using values 60° for θ_0 and 6 for *k* in equation C.2.

Appendix D. Scope of Curvature Based Ridge and Valleys Detection Techniques

Curvature of an image function is a measure of the 'bend' in the cross-section profile along a particular direction of the image intensity values. Hence, analysis of curvature based feature detection technique can be done using just 1D functions which represent the (cross-section) profiles of the features of interest. In this appendix, we present an analysis of the curvature based ridge/valley detection techniques using 1D profiles of ridges and valleys.

A ridge/valley detection technique detects medial lines of such structures. Such medial lines are loci of 'medial points' of the cross-section profiles of ridges/valleys. Therefore, in order to use 1D profile functions to perform an analysis of curvature based ridge/valley detection, the original 2D technique has to be reformulated to detect medial points of 1D profile functions. Before presenting such a reformulation, we shall define a few terms for ease of presentation later in this paper and state a Lemma.

Definition D.1 (Point of Magnitude Maximum): Let $f : \Re \rightarrow \Re$ be a 1D function. If a point $x = a$ is a point of local maximum of the function $y = \left| f(x) \right|$, then it is a point of magnitude maximum of the function $y = f(x)$. For brevity, we shall refer to such a point of magnitude maximum of a function as a **PMMAX** of the function.

Definition D.2 (Point of Magnitude Minimum): Let $f : \Re \rightarrow \Re$ be a 1D function. If a point $x = a$ is a point of local minimum of the function $y = \left| f(x) \right|$, then it is a point of magnitude minimum of the function $y = f(x)$. For brevity, we shall refer to such a point of magnitude minimum of a function as a **PMMIN** of the function.

Lemma D.1: Let $f : \Re \rightarrow \Re$ be a 1D function for which derivatives upto the second order exist. If

$$\text{(a)} \left[\frac{dy}{dx} \right]_{x=a} = 0 \text{ and, (b)} \left[y \frac{d^2y}{dx^2} \right]_{x=a} < 0$$

then, $x = a$ is a PMMAX of the function $y = f(x)$.

Proof:

$$f'(a) = 0,\ f(a) f''(a) < 0$$

$$\Rightarrow\ f(a) < 0,\ f'(a) = 0,\ f''(a) > 0$$

or

$f(a) > 0,\ f'(a) = 0,\ f''(a) < 0$

$\Rightarrow$ $f(a) < 0,\ f(a) < f(b),\ b \in (a-\delta, a+\delta) - \{a\}$ for some $\delta > 0$. (Since $f'(a) = 0,\ f''(a) > 0$ implies that $x = a$ is a point of minimum of $f(x)$)

or

$f(a) > 0,\ f(a) > f(b),\ b \in (a-\delta, a+\delta) - \{a\}$ for some $\delta > 0$. (Since $f'(a) = 0,\ f''(a) < 0$ implies that $x = a$ is a point of maximum, of $f(x)$)

$\Rightarrow$ $\left|f(a)\right| > \left|f(b)\right|,\ b \in (a-\delta, a+\delta) - \{a\}$ for some $\delta > 0$.

$\Rightarrow$ $x = a$ is a point of maximum of the function $y = \left|f(x)\right|$.

Hence, Lemma D.1 is proved. □

The curvature of a 1D function $y = f(x)$ is given as [17]:

$$\kappa(x) = \frac{\frac{d^2y}{dx^2}}{\left\{1 + \left(\frac{dy}{dx}\right)^2\right\}^{\frac{3}{2}}} \tag{D.1}$$

We shall now state the criterion for curvature based medial point detection using Definition D.1.

Definition D.3 (Curvature based criterion for medial points of 1D profile functions): Let $f : \Re \rightarrow \Re$ be a 1D function for which derivatives upto the second order exist. A point $x = a$ is a medial point of the profile function $y = f(x)$ if it is a PMMAX of $\kappa(x)$.

The PMMAX of the curvature is where the derivative of the curvature vanishes. The derivative of the curvature is found, by differentiating the expression in equation D.1:

$$\frac{d\kappa}{dx} = \frac{\frac{d^3y}{dx^3}\left\{1 + \left(\frac{dy}{dx}\right)^2\right\} - 3\,\frac{dy}{dx}\left(\frac{d^2y}{dx^2}\right)^2}{\left\{1 + \left(\frac{dy}{dx}\right)^2\right\}^{\frac{5}{2}}} \tag{D.2}$$

Considering equation D.2, it is clear that the first derivative of the curvature can vanish under four

different conditions. These are:

C1 :: $\frac{dy}{dx} = 0,\ \frac{d^2y}{dx^2} \neq 0,\ \frac{d^3y}{dx^3} = 0$

C2 :: $\frac{dy}{dx} = 0,\ \frac{d^2y}{dx^2} = 0,\ \frac{d^3y}{dx^3} = 0$

C3 :: $\frac{dy}{dx} \neq 0,\ \frac{d^2y}{dx^2} = 0,\ \frac{d^3y}{dx^3} = 0$

C4 :: $\frac{dy}{dx} \neq 0,\ \frac{d^2y}{dx^2} \neq 0,\ \frac{d^3y}{dx^3} \neq 0$ but the numerator as a whole, of the expression on the right hand side of equation D.2, goes to zero.

The second derivative of the profile function is zero in C2 and C3. Hence, by equation D.1, the curvature of the profile function also goes to zero at such points. Therefore, a point satisfying C2 or C3 cannot be a PMMAX of the curvature function. A medial point is either the top of a ridge profile, or the bottom of a valley profile. In other words, the medial points are points of extremal image intensities. Hence, a PMMAX which satisfies C4 cannot be a medial point of a ridge/valley profile. Such PMMAX occur as 'knee/elbow' points of edge profiles, as shown in Figure D.1. In practice, it is either rejected by setting a threshold or in few rare cases, is wrongly classified as a ridge/valley pixel. Therefore, medial points which satisfy the criterion in Definition D.3 should satisfy only C1. However, a point satisfying C1 need not satisfy the criterion in Definition D.3. The following theorem gives us a condition under which a point satisfying C1 is also a PMMAX of the curvature function.

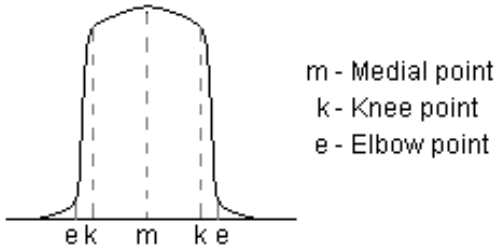

Figure D.1. Cross-section of a ridge and the various points of extremal curvature.

Theorem D.1: Let $f : \Re \rightarrow \Re$ be a 1D function for which derivatives upto the fourth order exist. If for some point $x = a$, we have $\left[\frac{dy}{dx}\right]_{x=a} = 0$, $\left[\frac{d^2y}{dx^2}\right]_{x=a} \neq 0$, $\left[\frac{d^3y}{dx^3}\right]_{x=a} = 0$, and

$$\left[\frac{d^2y}{dx^2} \left\{ \frac{d^4y}{dx^4} - 3\left(\frac{d^2y}{dx^2}\right)^3 \right\} \right]_{x=a} < 0 \tag{D.3}$$

then, $x = a$ is a PMMAX of the curvature of function $y = f(x)$.

Proof: Follows trivially by applying Lemma D.1 to the curvature expression in equation D.1 □

If at some point on the profile, the fourth-derivative is non-zero; the curvature function has a PMMAX; and C1 is satisfied; then, the profile function has to satisfy an inequality. This is stated in the following theorem.

Theorem D.2: Let $f : \Re \to \Re$ be a 1D function for which derivatives upto fourth order exist. If some point $x = a$ is a PMMAX of the curvature of the function $y = f(x)$ while satisfying $\left[\frac{dy}{dx}\right]_{x=a} = 0$, $\left[\frac{d^2y}{dx^2}\right]_{x=a} \neq 0$, $\left[\frac{d^3y}{dx^3}\right]_{x=a} = 0$ and $\left[\frac{d^4y}{dx^4}\right]_{x=a} \neq 0$, then

$$\left[\frac{d^2y}{dx^2} \left\{ \frac{d^4y}{dx^4} - 3\left(\frac{d^2y}{dx^2}\right)^3 \right\} \right]_{x=a} < 0 \tag{D.4}$$

Proof: The Taylor's series approximation of the function $\frac{d^2y}{dx^2}$ upto the second derivative, in a neighbourhood of the point $x = a$, under the conditions of the theorem is:

$$\frac{d^2y}{dx^2} = \left[\frac{d^2y}{dx^2}\right]_{x=a} + \frac{(x-a)^2}{2}\left[\frac{d^4y}{dx^4}\right]_{x=a} \tag{D.5}$$

Similar approximation for the function $\left\{1 + \left(\frac{dy}{dx}\right)^2\right\}^{\frac{3}{2}}$, under the conditions of the threorem, is:

$$\left\{1 + \left(\frac{dy}{dx}\right)^2\right\}^{\frac{3}{2}} = 1 + \frac{3}{2}(x-a)^2\left[\left(\frac{d^2y}{dx^2}\right)^2\right]_{x=a} \tag{D.6}$$

Hence, the curvature expression from equation D.1 can be approximated, in the neighbourhood of $x = a$, as:

$$\kappa(x) = \frac{\left[\frac{d^2y}{dx^2}\right]_{x=a} + \frac{(x-a)^2}{2}\left[\frac{d^4y}{dx^4}\right]_{x=a}}{1 + \frac{3}{2}(x-a)^2\left[\left(\frac{d^2y}{dx^2}\right)^2\right]_{x=a}} \tag{D.7}$$

Let $\left[\frac{d^2y}{dx^2}\right]_{x=a} > 0$. Since $x = a$ is a PMMAX of the curvature function, for an x in a small neighbourhood of $x = a$, we must have:

$$\kappa(x) < \kappa(a) \tag{D.8}$$

Substituting for the expression of $\kappa(x)$ from equation D.7 into the inequality D.8 and re-arranging, we get:

$$\left[\frac{d^4y}{dx^4}\right]_{x=a} - 3\left[\left(\frac{d^2y}{dx^2}\right)^3\right]_{x=a} < 0 \tag{D.9}$$

If $\left[\frac{d^2y}{dx^2}\right]_{x=a} < 0$, we can arrive at similar inequality as:

$$\left[\frac{d^4y}{dx^4}\right]_{x=a} - 3\left[\left(\frac{d^2y}{dx^2}\right)^3\right]_{x=a} > 0 \tag{D.10}$$

Combining inequalities D.9 and D.10, by taking into consideration the sign of the second-derivative at $x = a$, we get:

$$\left[\frac{d^2y}{dx^2}\left\{\frac{d^4y}{dx^4} - 3\left(\frac{d^2y}{dx^2}\right)^3\right\}\right]_{x=a} < 0 \tag{D.11}$$

Hence, Theorem D.2 is proved. □

C1 requires the third-derivative to be zero while the second-derivative is non-zero. Let $x = a$ be a point where C1 occurs. Then, we will have the following possible properties for the second-derivative function at that point.

A. $x = a$ **is a PMMAX of the second-derivative function:**

Since the denominator of the curvature expression (equation D.1) is always positive, the point $x = a$ is a PMMIN of the denominator of the curvature expression. Furthermore, given that the point $x = a$ is a PMMAX of the second-derivative implies that it is also a PMMAX of the numerator of the curvature expression. Therefore, we can conclude that $x = a$ is a PMMAX of the curvature expression as a whole.

B. **$x = a$ is a point of inflection of the second-derivative function which is non-zero at this point:**

In this case, we must have $\left[\frac{d^4y}{dx^4}\right]_{x=a} = 0$. Hence, we have

$$\left[\frac{d^2y}{dx^2}\left\{\frac{d^4y}{dx^4} - 3\left(\frac{d^2y}{dx^2}\right)^3\right\}\right]_{x=a}$$

$$= \left[\left\{-3\left(\frac{d^2y}{dx^2}\right)^4\right\}\right]_{x=a} < 0$$

Therefore, by Theorem D.1, the point $x = a$ is also a PMMAX of the curvature function. An example of a profile function with such a PMMAX is $f(x) = x^5 + 10x^2$, $x \in [-1, 1]$ and its second derivative is $f''(x) = 20x^3$. $x = 0$ is a point of inflection of the second-derivative, which is also a PMMAX of its curvature function.

C. **The second-derivative is a non-zero constant function:**

In this case again, the fourth derivative must vanish, i.e., $\left[\frac{d^4y}{dx^4}\right]_{x=a} = 0$. Hence, as in case B above, the point $x = a$ is a PMMAX of the curvature function. Examples of such profiles are quadratic polynomials which have a unique point of minimum or maximum.

D. **$x = a$ is a PMMIN of the second-derivative function which is non-zero here; the fourth derivative vanishes at this point:**

Using Theorem D.1 again, as with cases B and C above, it can be concluded that $x = a$ is a PMMAX of the curvature function.

E. **$x = a$ is a PMMIN of the second-derivative function and the fourth and the second derivatives are non-zero at this point:**

Using Theorems D.1 and D.2, $x = a$ is a PMMAX of the curvature function only if the derivatives of the profile function satisfy the inequality D.4.

The five different cases discussed above correspond to five classes of profiles for which a point satisfying C1 is also a PMMAX of the curvature function. Hence, we conclude that there are five different classes of ridge and valley profiles which can be detected by techniques using the curvature based criterion in Definition D.3. These classes are summarised below for easy reference, in terms of the characteristics of the function at the medial point.

Class 1 Functions for which there exists a PMMAX of the second-derivative at a point where the first derivative vanishes.

Class 2 Functions for which there exists a point of inflection of the second-derivative at a point where the first-derivative vanishes and the second-derivative has a non-zero value.

Class 3 Functions for which the second-derivative is a non-zero constant function and there exists a point where the first derivative vanishes.

Class 4 Functions for which there exists a PMMIN of the second-derivative at a point where the first and fourth derivatives vanish, and the second-derivative has a non-zero value.

Class 5 Functions for which there exists a PMMIN of the second-derivative at a point where the fourth-derivative is non-zero, and condition C1 and the inequality D.4 are satisfied at that point.

References

[1] American Diabetes Association. All About Diabetes. URL *http://www.diabetes.org/about-diabetes.jsp.*

[2] Abdel Azeem, S., Hafez, M., andAuda, G.. Using Circular Hough Transform for Detecting Microaneurysms in Fluorescein Angiogram of the Ocular Fundus. *In proceeding of the International Conference on Industrial Electronics, Technology and Automation* (Dec. 2001).

[3] J. Canny. A Computational Approach to Edge Detection. *IEEE Transactions on Pattern Analysis and Machine Intelligence, Volume 8, Issue 6* (November 1986).

[4] Michael J. Cree, John A. Olson, Kenneth C. McHardy, Peter F. Sharp, John V. Forrester. Automated Microaneurysm Detection. *IEEE International Conference on Image Processing* (1996).

[5] Michael J. Cree, John A. Olson, Kenneth C. McHardy, Peter F. Sharp, John V. Forrester. The Preprocessing of Retinal Images for the Detection of Fluorescein Leakage. *Phy. Med. Biol.44 (1999) 293-308* (1999).

[6] Diabetesindia.com. Diabetes. URL *http://www.diabetesindia.com.*

[7] Dictionary.com. Retina. URL *http://dictionary.reference.com/search?q=Retina.*

[8] Charles V. Stewart, Chia-Ling Tsai, Badrinath Roysam. The Dual Bootstrap Iterative Closest Point Algorithm with Application to Retinal Image Registration, RPI. Tech. Rep. (2003).

[9] D. Eberly, R. Gardner, B. Morse, S. Pizer, C. Scharlach. Ridges for image analysis. *Journal of Mathematical Imaging and Vision, 4:353-373* (1994).

[10] Rafael C. Gonzalez, Richard E. Woods. *Digital Image Processing.* Pearson Education. Second Edition, Fifth Indian Reprint, 2002.

[11] Mohammed Hafez, Sherif Abdel Azeem. Using Adaptive Edge Technique for Detecting Microaneurysms in Flourescein. *IEEE MELECON 2002, Cairo, Egypt* (May 7-9, 2002).

[12] R. Haralick. Ridges and Valleys on Digital Images. *Computer Vision, Graphics and Image Processing, 22:28-38* (1983).

[13] Adam Hoover. Equalizing Illumination in a Retinal Image Using Blood Vessels as a Reference. Tech. Rep. (2000). URL *http://www.parl.clemson.edu/stare/eq/* .

[14] Heidelbergengineering.com. Heidelberg Engineering. URL *http://www.heidelbergengineering.com.*

[15] F. F. Jana, J. C. Klein. Segmentation of vessel like patterns using mathematical morphology and curvature evaluation. *IEEE Transactions on Medical Imaging, 10(7), 1010-1019* (2001).

[16] Eric R. Kandel, James H. Schwartz, Thomas M. Jessell. *Principles of Neural Science.* McGraw-Hill Medical, 2000.

[17] Erwin Kreyszig. *Advanced Engineering Mathematics.* Wiley. Eight Edition, 1998.

[18] A. Lopez, F. Lumbreras, J. Serrat and J. Villanueva. Evaluation of methods for ridge and valley detection. *IEEE Trans. on PAMI, 21(4):327-335* (1999).

[19] J. B. A. Maintz, P. A. van den Elsen, M. A. Viergever. Evaluation of Ridge Seeking Operators for Multimodality Medical Image Matching. *IEEE Trans. on PAMI, 18(4)* (1996).

[20] A. M. Mendonca, A. J. Campilho, J. M. Nunes. Automatic Segmentation of Microaneurysms in Retinal Angiograms of Diabetic Patients. *International Conference on Image Analysis and Processing* (1999).

[21] O. Monga, N. Armande, P. Montesinos. Thin nets and Crest lines: Applications to Satellite Data and Medical Images. *Proceeding of the IEEE Intl. Conf. of Image Procc.* (1995).

[22] Jeffrey W. Berger, Michael E. Leventon, Nobuhiko Hata, William Wells, Ron Kikinis. Design Considerations for Computer-Vision-Enabled Opthalmic Augmented Reality Environment, MIT. Tech. Rep. (1996).

[23] G. Osterberg. *Topography of the layer of rods and cones in the human retina.*

[24] Adam Hoover, Valentina Kouznetsova, Michael Goldbaum. Locating Blood Vessels in Retinal Images by Piecewise Threshold Probing of a Matched Filter Response. *IEEE Transaction on medical imaging, Vol.19, No.3* (March 2000).

[25] MathWorld. Principal Curvatures. URL *http://mathworld.wolfram.com/PrincipalCurvatures.html*.

[26] Ali Can, Hong Shen, James N. Turner, Howard L. Tanenbaum, Badrinath Roysam. Rapid Automated Tracing and Feature Extraction from Retinal Fundus Images Using Direct Exploratory Algorithms. *IEEE Transactions on Information Technology in Biomedicene, Vol. 3, No.2* (1999).

[27] J. Serrat, A. Lopez, D. Lloret. On Ridges and valleys. *Proceeding of the 15th International Conference on Pattern Recognition* (2000).

[28] T. Spencer, John A. Olson, Kenneth C. McHardy, Peter F. Sharp, John V. Forrester. An image-processing strategy for the segmentation and quantification of microaneurysms in fluorescein angiograms of the ocular fundus. *Computer and Biomedical Research, vol 29, pp 284-302* (1996).

[29] P. H. Gregson, Z. Shen, R. C. Scott, V. Kozousek. Automated Grading of Venous Beading. *Computers and Biomedical Research 28, 291-304* (1995).

[30] Subhasis Chaudhari, Shankar Chatterjee, Norman Katz, Mark Nelson, Michael Goldbaum. Detection of blood vessels in retinal images using two-dimensional matched filters. *IEEE Transaction on medical imaging, Vol.8, No.3, September 1989* (1989).

[31] W. E. Hart, P. Kube, M. Goldbaum. Automatic measurement of retinal vascular tortuosity. *Tech. Report, Dept. Elec and Comp. Engg., Univ. of California, San Diego.*

[32] Haitao Wang, Stan Z. Li, Yangsheng Wang. Generalised Quotient Image. *IEEE Computer Society Conference in Computer Vision and Pattern Recognition* (2004).

[33] Haitao Wang, Stan Z. Li, Yangsheng Wang, Jianjun Zhang. Self Quotient Image for Face Recognition. *IEEE International Conference on Image Processing* (2004).

[34] wxWidgets.org. wxWidgets - The open source, cross-platform native UI framework. URL *http://wxwidgets.org.*

[35] Zeiss.com. Carl Zeiss International. URL *http://www.zeiss.com.*

[36] Juhua Zhu, Bede Liu, Stuart C. Schwartz. General Illumination Correction and its Application to Face Normalisation. *IEEE International Conference on Acoustics, Speech and Signal Processing* (2003).